JPL Publication 258499

Hyperspectral Thermal Emission Spectrometer (HyTES) Level-2 Land Surface Temperature and Emissivity Algorithm Theoretical Basis Document

G. Hulley
S. Hook
W. Johnson
P. Guillevic
N. Malakar

Jet Propulsion Laboratory, California Institute of Technology

National Aeronautics and Space Administration

Jet Propulsion Laboratory
California Institute of Technology
Pasadena, California

May 2016

This research was carried out at the Jet Propulsion Laboratory, California Institute of Technology, under a contract with the National Aeronautics and Space Administration.

Change History Log

Revision	Effective Date	Prepared by	Description of Changes
Draft	05/07/2016	Glynn Hulley	First Draft and outline
Draft	05/20/2016	Nabin Malakar	Included PC regression details
Draft	05/23/2016	Glynn Hulley	Added example images and retrieved spectra, and validation.

Contacts

Readers seeking additional information about this study may contact the following researchers:

Glynn C. Hulley
MS 183-501
Jet Propulsion Laboratory
4800 Oak Grove Dr.
Pasadena, CA 91109
Email: glynn.hulley@jpl.nasa.gov
Office: (818) 354-2979

Simon J. Hook
MS 183-501
Jet Propulsion Laboratory
4800 Oak Grove Dr.
Pasadena, CA 91109
Email: simon.j.hook@jpl.nasa.gov
Office: (818) 354-0974

Abstract

The Hyperspectral Thermal Emission Spectrometer (HyTES) is a new airborne imaging spectrometer developed by the NASA Jet Propulsion Laboratory. HyTES has 256 contiguous spectral channels between 7.5 and 12 µm and a 50 degree total field of view. The instrument has an instantaneous field of view of 1.7066 milliradians with pixel size dependent on flight altitude. Currently the instrument operates on a Twin Otter aircraft with plans underway to modify the instrument so that it can also be flown on the NASA ER2 in early 2016. The Twin Otter is a low altitude aircraft and the ER2 is a high altitude aircraft. The two aircraft allow the acquisition of data with pixel sizes between 1.7 m (1 km above surface) and 34 m (20 km above surface). HyTES is the first high spatial and high spectral resolution thermal infrared imaging spectrometer developed by NASA. HyTES measurements are made possible through the incorporation of many advanced technologies including a Dyson spectrometer, convex diffraction grating and Quantum Well Infrared Photodetector (QWIP). HyTES was developed to provide exemplar datasets at high spatial and spectral resolutions that could be resampled to determine the optimum band positions for the thermal infrared (TIR) instrument that is part of the Hyperspectral Infrared Imager (HyspIRI) concept. A prototype instrument of the TIR has been developed referred to as the Prototype HyspIRI Thermal Infrared Radiometer (PHyTIR). In 2014 a proposal to deploy PHyTIR on the International Space Station was selected. That mission uses the modified PHyTIR instrument to measure evapotranspiration and is referred to as the ECOsystem Spaceborne Thermal Radiometer Experiments on Space Station (ECOSTRESS) and scheduled for launch in 2017. HyTES had its initial engineering flights in 2012 and first science flights in 2013. HyTES has now had several successful deployments and used to produce HyspIRI-like datasets as well as conduct new science only possible due to its combined high spatial and spectral resolution. For example the mapping of methane emissions from a variety of sources such as dairies, natural seeps, landfills and oil and gas infrastructure. All these datasets are freely available from the HyTES website (http://hytes.jpl.nasa.gov). Here we provide a detailed description of the instrument and its performance both in the laboratory as well as in airborne validation experiments together with examples of using the data for a variety of applications from surface mineral mapping to characterizing methane plumes.

Contents

Figures

Tables

1 Introduction

In 2007 the National Research Council (NRC) released the results from the first Earth Science Decadal Survey in a report titled *Earth Science and Applications from Space: National Imperatives for the next Decade and Beyond* (NRC 2007). The purpose of DS study was to provide NASA with a mission roadmap for the subsequent 10 years together with the high priority science and societal questions that needed to be addressed. The report identified key science measurements and recommended a small number of missions to acquire those measurements. The missions were arranged in three groups or tiers referred to as the Tier I, Tier II or Tier III missions. One of the missions recommended in the Tier II group was The Hyperspectral and Infrared Imager (HyspIRI).

The HyspIRI mission includes a visible-shortwave infrared (VSWIR) imaging spectrometer and a multispectral thermal infrared (TIR) scanner together with an onboard data processing/downlink system referred to as the Intelligent Payload Module (IPM) (HyspIRI Group, 2009, Abrams and Hook 2013). The VSWIR instrument will obtain a contiguous spectrum in each pixel from 0.38 and 2.5 µm with 10 nm sampling. The TIR instrument will acquire data in 8 discrete spectral bands between 4 and 12 µm for each pixel. In the initial concept of the HyspIRI mission the VSWIR instrument had a revisit of 19 days and a spatial resolution of 60 m. In the latest version of the HyspIRI concept the VSWIR instrument will have a revisit of 16 days and a spatial resolution of 30 m (Lee et al. 2015). The TIR instrument will continue to have a revisit of 5 days and 60 m, although that may change as the technology continues to mature. Both instruments will provide global observations over the land surface and surrounding shallow waters. Over the deeper oceans the data will be resampled to 1 km spatial resolution. NASA assigned the Jet Propulsion Laboratory (JPL) to lead the HyspIRI mission concept study with support from the Goddard Space Flight Center (GSFC). Drs. Simon Hook, Robert Green and Elizabeth Middleton were assigned responsibility for the TIR, VSWIR and IPM respectively.

The HyspIRI-TIR instrument is a multispectral TIR scanner with 8 spectral bands. Seven of the eight bands are between 7.5 and 12 µm and the remaining band is at 4 µm. The 4 µm band is specifically designed for the detection of hot targets (Abrams and Hook 2013). As part of the TIR risk reduction studies the NASA Earth Science Technology Office (ESTO) supported the

development of an airborne Hyperspectral Thermal Emission Spectrometer (HyTES) and the Prototype HyspIRI Thermal Infrared Radiometer (PHyTIR) for science and engineering risk reduction respectively (Hook et al. 2011, Hook et al. 2013). HyTES acquires data at much higher spatial and spectral resolutions than HyspIRI-TIR for science studies and to identify the optimum positions for the spectral filters for 7 of the 8 bands on the HyspIRI-TIR instrument. The higher spatial and spectral resolution of HyTES ensures the HyTES data can be resampled to provide HyspIRI-TIR like data or used to conduct studies which require high spectral resolution data such as gas studies. The PHyTIR instrument was developed to demonstrate that the HyspIRI-TIR hardware would perform correctly in a space environment. PHyTIR was a space-flight ready laboratory engineering model (Hook et al. 2011). In 2014 PHyTIR was selected for deployment to the International Space Station (ISS) as part of the ECOsystem Spaceborne Thermal Radiometer Experiment on Space Station (ECOSTRESS) mission (Lee et al. 2015).

HyTES was selected for development in 2007 under the ESTO Instrument Incubator Program (IIP) and work began on the instrument in 2008. HyTES had its first engineering flights in 2012; these flights demonstrated the instrument operated as planned and work continued on the instrument supported by the NASA Research and Analysis (R&A) program and HyTES had its first science flights in 2013 (Hook et al. 2013). HyTES has 256 contiguous spectral channels between 7.5 and 12 µm. HyTES incorporates several new technologies including a Dyson spectrometer, Quantum Well Infrared Photodetector (QWIP) and a curved diffraction grating (Hook et al. 2013). It should be emphasized that the HyspIRI-TIR instrument design is different to the HyTES design. The HyspIRI-TIR uses a scan mirror to acquire a wide swath of imagery but in a limited number of spectral bands whereas the HyTES uses a pusbroom design that allows a greater dwell time and signal throughput enabling more spectral bands than HyspIRI-TIR but for a narrower swath. The higher spectral resolution data from HyTES can be used to both discriminate and identify materials which may not be possible with a smaller number of discrete spectral channels. Selected characteristics of thermal infrared measurements made by HyspIRI, HyTES and ECOSTRESS are given in Table 1.

Table 1: HyspIRI, HyTES and ECOSTRESS specifications

Instrument Characteristics	Unit	HyspIRI	HyTES	ECOSTRESS
Number of cross track pixels	count	9840	512	5400
Number of bands	count	8	256	6
Spectral range	μm	4-12.5	7.5-12	2-12.5
Typical dwell time	μs	32	44000	32
Total field of view	degrees	51	50	53
Calibration	n/a	1 on-board blackbody/ 1 Space view	pre and post flight blackbody and spectral	2 on-board blackbodies
Detector array size	count	256x128	1024x1024	256x128
Detector array pitch	count	40	19.5	40
Detector temperature	Kelvin	60	40	65
Optics temperature	Kevlin	300	100	310
Slit width	μm	N/A	39	N/A
Pixel projection on ground	m	60x60	1.3-36.4	38x68

Maximum radiometric emission for the typical range of Earth surface temperatures, excluding fires and volcanoes, is found in two infrared spectral "window" regions: the midwave infrared (3.5–5 μm) and the thermal infrared (8–13 μm). The radiation emitted in these windows for a given wavelength is a function of both temperature and emissivity. Determining the separate contribution from each component in a radiometric measurement is an ill-posed problem since there will always be more unknowns—N emissivities and a single temperature—than the number of measurements, N, available. For HyTES, we will be solving for one temperature and six emissivities (HyTES TIR window bands 54-256). Therefore, an additional constraint is needed, independent of the data. There have been numerous theories and approaches over the past two decades to solve for this extra degree of freedom. For example, the ASTER Temperature Emissivity Working Group (TEWG) analyzed ten different algorithms for solving the problem (Gillespie et al. 1999). Most of these relied on a radiative transfer model to correct at-sensor radiance to surface radiance and an emissivity model to separate temperature and emissivity. Other approaches include the split-window (SW) algorithm, which extends the SST SW approach to land surfaces, assuming that land emissivities in the window region (10.5–12 μm) are stable and well known. However, this assumption leads to unreasonably large errors over barren regions where emissivities have large variations both spatially and spectrally. The ASTER TEWG finally decided on a hybrid algorithm, termed the temperature emissivity

separation (TES) algorithm, which capitalizes on the strengths of previous algorithms with additional features (Gillespie et al. 1998).

TES is applied to the land-leaving TIR radiances that are estimated by atmospherically correcting the at-sensor radiance on a pixel-by-pixel basis using a radiative transfer model. TES uses an empirical relationship to predict the minimum emissivity that would be observed from a given spectral contrast, or minimum-maximum difference (MMD) (Kealy and Hook 1993; Matsunaga 1994). The empirical relationship is referred to as the calibration curve and is derived from a subset of spectra in the ASTER spectral library (Baldridge et al. 2009). A new calibration curve, applicable to HyTES TIR window bands, will be computed from the ASTER spectral library. TES has been shown to accurately recover temperatures within 1.5 K and emissivities within 0.015 for a wide range of surfaces and is a well established physical algorithm that produces seamless images with no artificial discontinuities such as might be seen in a land classification type algorithm (Gillespie et al. 1998).

The remainder of the document will discuss the HyTES instrument characteristics, provide a background on TIR remote sensing, give a full description and background on the atmospheric correction and TES algorithm, provide quality assessment, discuss numerical simulation studies and, finally, outline a validation plan.

2 HyTES Instrument Characteristics

The following description of the instrument is summarized from Hook et al. (2013). In 2005 several recent technological developments such as Quantum Well Infrared Photodetector (QWIP) arrays, commercial off the shelf (COTS) coolers, Dyson spectrometer designs and curved electron microbeam diffraction gratings suggested the possibility of developing a compact wide swath hyperspectral thermal infrared imaging spectrometer with a detector cooled to 40 Kelvin. In order test this possibility JPL developed a pushbroom hyperspectral thermal infrared breadboard instrument termed the Quantum Well Earth Science Testbed (QWEST) as a laboratory demonstration. QWEST brought together numerous in-house specialties such as optical design and general spectrometer alignment optimization, precision slit fabrication, high efficiency and low scatter concave diffraction grating design and fabrication, precision mechanical and machining capability and QWIP focal plane arrays. QWEST demonstrated an

instrument could be developed and provide sufficient capability and in 2007 work began on the airborne HyTES instrument supported through the NASA Earth Science Technology Office (ESTO) Instrument Incubator Program (IIP).

HyTES uses a Dyson spectrometer which provides a concentric optical design and allows a point to be mapped perfectly to the focal plane array. Compared with other optical designs such as the Offner, the Dyson design is far more compact allowing the entire system to be placed in a dewar and cooled with mechanical cryocoolers. The HyTES optical design minimizes smile and keystone distortion while simultaneously virtually eliminating ghosting. The slit width of HyTES is 39 μm, which corresponds to two detector pixels. Smile and keystone distortions are kept to no more than 1-2% of this or ~2 μm. JPL can fabricate ultra-precision slits using reactive ion etching which can be kept straight to an order of magnitude better than this. For this reason the slit straightness is not typically the limiting factor in spectrometer performance. The Dyson spectrometer is manufactured from a single monolithic block which is used in double pass where light from the slit enters at a narrow optical passageway and is transmitted through the rear power surface, diffracts off the grating and re-enters the block to totally internally reflect off the back surface which guides the spectrally dispersed radiation to focus at the QWIP detector location, labeled as the Focal Plane Array (FPA) in Figure 1. The FPA is kept at 40 Kelvin.

The HyTES telescope is kept cold (100 K) minimizing any self-emission that would negatively impact the dynamic range, uniformity, and linearity of the data. HyTES uses a reflective off-axis two mirror anastigmat telescope which is a two-piece, self-aligning all aluminum design. The mirror surfaces in the telescope are over coated with gold for maximum reflectivity, and the telescope is baffled and internal surfaces painted with high emissivity black, to minimize stray light reflection. After the telescope and prior to the spectrometer housing HyTES has a relay assembly. The relay assembly minimizes stray light and allows for a fixed aperture stop position for the telescope. The assembly includes 6 lens elements held in a kinematic mount to minimize distortions during flight operation. The stop aperture is symmetrically placed between the two stacks of 3 lenses (Figure 1). This symmetric design allows the focused field rays from the telescope to be re-imaged at the spectrometer slit with essentially zero chromatic aberration. All optical surfaces are coated with highly transmissive interference layers in order to maximize light throughput and all other internal surfaces are coated with black paint.

Beyond the relay is the limit which limits the field angle and is followed by the Dyson spectrometer. The slits are manufactured at JPL by Reactive ion etching. The Dyson spectrometer was machined from a ZnSe block. Broadband area coatings are used on all applicable light transmitting surfaces. The coatings allow 99.0% or better long wave infrared light to transmit per surface. Collimated light passes through the spectrometer to a curved diffraction grating which disperses the light and re-transmits it to the Dyson spectrometer which reflects it to the detector. The diffraction grating is manufactured by JPL using electron-beam lithography techniques. These techniques allow fabrication of precisely blazed gratings on curved substrates having several millimeters of height variation (Wilson et al. 2003, Perry et al., 1993). To date, JPL is the only facility capable of producing electron beam fabricated gratings on curved substrates. Gratings fabricated in this manner have low scatter and are highly efficient.

HyTES uses a QWIP detector (Gunapala et al. 2007) and is the first integration of the QWIP with a spectrometer system for Earth science studies requiring accurately calibrated data. The detector pixel pitch of the FPA is 20 μm and the actual pixel area is 19.5x19.5 μm. Indium bumps were evaporated on top of the detectors for hybridization with a silicon readout integrated circuit (ROIC). These QWIP FPAs were hybridized (via indium bump-bonding process) to a 1024x1024 pixel complementary metal-oxide semiconductor (CMOS) ROIC. The QWIP is known for its high spatial uniformity (<1%) and relatively low manufacturing cost. QWIP's typically cover a relatively narrow wavelength band (~1 μm bandwidth) to overcome this limitation JPL created a 2-stack QWIP allowing the spectral range to be extended from 7.5 -12 μm. The focal plane array format is 1024x1024 pixels. The spectral dispersion covers only half of the array (i.e. 1024x512). The cross track spatial light is spread out across the 1024 pixel direction while the spectral channels are along the 512 direction. The pixels are binned 2x2 in software during post processing to form one effective pixel. This allows the signal to noise and operability to be improved.

The entire optical system and detector is housed in a cryovacuum chamber to minimize self-emission which is cooled with two mechanical cryocoolers. One cryocooler maintains the focal plane temperate at 40 K while the other maintains the optical system at 100 K. The focal plane reaches its operating temperature in about 4 hours whereas the rest of the system takes about 5 days to reach operating temperature. For this reason the instrument is typically cooled before a

deployment and shipped cold and then installed on the aircraft when it is already cooled to temperature.

Currently HyTES is only deployed on the Twin Otter aircraft, however, modifications are underway to enable deployment on the ER2. Figure 2 shows an example HyTES data hypercube over Death Valley, California. Radiances in the vertical slice have been atmospherically corrected for the atmospheric transmission and path radiance. Figure 3 show the instrument deployed in Twin Otter.

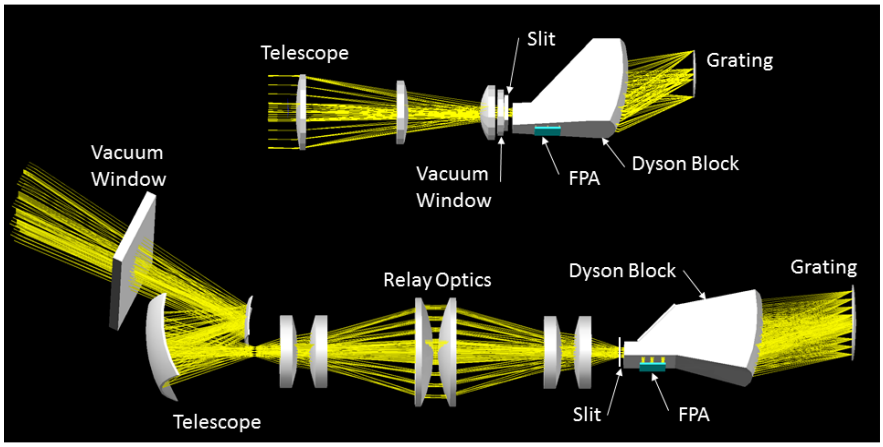

Figure 1. Optical ray trace of the QWEST Dyson spectrometer and objective lens elements. Thermal radiation passes through the slit and is dispersed by the grating. The dispersed light is ultimately reimaged back at the focal plane array (FPA) which is kept at 40 K to obtain the optimum performance from the detector. Figure 1-bottom. Optical ray trace of Dyson spectrometer and objective lens elements. Thermal radiation passes through the slit and is dispersed by the grating. The dispersion is reimaged ultimately back at the focal plane array.

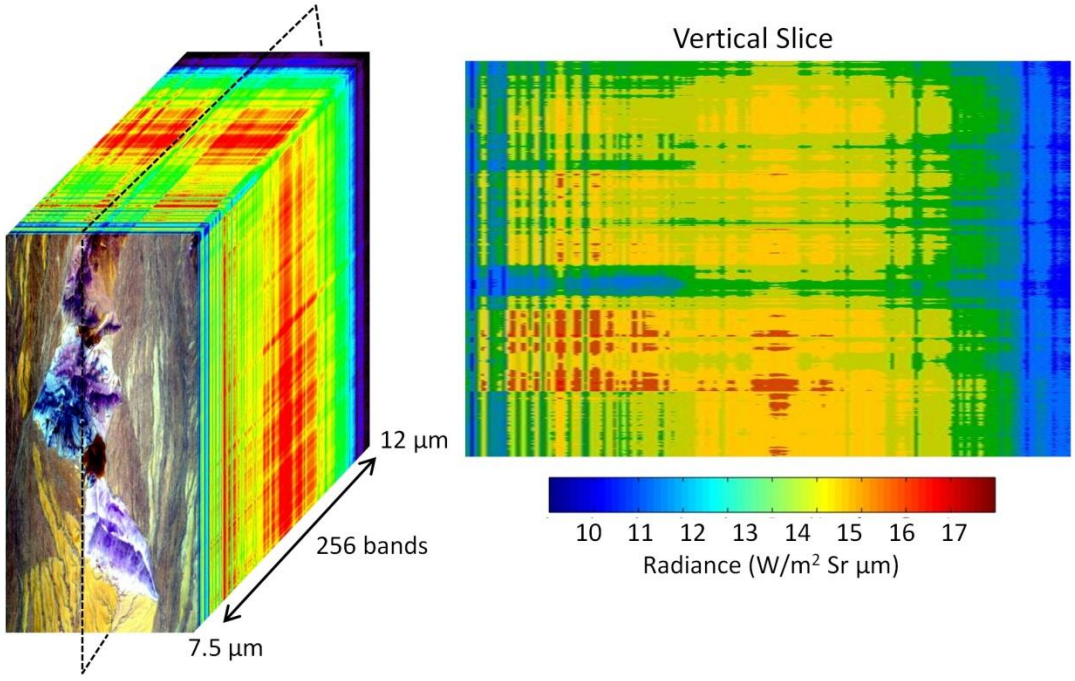

Figure 2. HyTES data hypercube over Death Valley, California. Radiances in the vertical slice have been atmospherically corrected for the atmospheric transmission and path radiance.

Figure 3. HyTES installation in Twin Otter aircraft.

3 Theory and Methodology

3.1 TIR Remote-Sensing Background

The at-sensor measured radiance in the TIR spectral region (8–14 μm) is a combination of different terms from surface emission and the atmosphere. The Earth-emitted radiance is a function of temperature and emissivity and gets attenuated by the atmosphere on its path to the satellite. The atmosphere also emits radiation, of which some reaches the sensor directly as "path radiance," while some gets radiated to the surface (irradiance) and reflected back to the sensor, commonly known as the reflected downwelling sky irradiance. One effect of the sky irradiance is the reduction of the spectral contrast of the emitted radiance, due to Kirchhoff's law. Assuming the spectral variation in emissivity is small (Lambertian assumption), and using Kirchhoff's law to express the hemispherical-directional reflectance as directional emissivity ($\rho_\lambda = 1 - \epsilon_\lambda$), the clear sky at-sensor radiance can be written as three terms: the Earth-emitted radiance described by Planck's function and reduced by the emissivity factor, ϵ_λ; the reflected downwelling irradiance; and the path radiance.

$$L_\lambda(\theta) = \left[\epsilon_\lambda B_\lambda(T_s) + (1-\epsilon_\lambda)L_\lambda^{\downarrow}\right]\tau_\lambda(\theta) + L_\lambda^{\uparrow}(\theta) \quad (1)$$

$L_\lambda(\theta)$ = at-sensor radiance;

λ = wavelength;

θ = observation angle;

ϵ_λ = surface emissivity;

T_s = surface temperature;

$L_\lambda^{\downarrow}$ = downwelling sky irradiance;

$\tau_\lambda(\theta)$ = atmospheric transmittance;

$L_\lambda^{\uparrow}(\theta)$ = atmospheric path radiance

$B_\lambda(T_s)$ = Planck function, described by Planck's law:

$$B_\lambda = \frac{c_1}{\pi\lambda^5}\left(\frac{1}{\exp\left(\frac{c_2}{\lambda T}\right) - 1}\right) \quad (2)$$

$c_1 = 2\pi hc^2$=3.74· 10^{-16} W·m^2 (1st radiation constant)

h = 6.63· 10^{-34} W·s^2 (Planck's constant)

c2 = h·c/k = 1.44× 10^4 μm·K (2nd radiation constant)

k = 1.38× 10^{-23} W·s·K^{-1} (Boltzmann's constant)

c = 2.99· 10^8 m·s^{-1} (speed of light)

Figure 4 shows the relative contributions from the surface-emission term, surface radiance, and at-sensor radiance for a US Standard Atmosphere, quartz emissivity spectrum, and surface temperature set to 300 K. Vertical bars show the placement of the eight HyspIRI MWIR and TIR bands. The reflected downwelling term adds a small contribution in the window regions but will become more significant for more humid atmospheres. The at-sensor radiance shows large departures from the surface radiance in regions where atmospheric absorption from gases such as CO_2, H_2O, and O_3 are high.

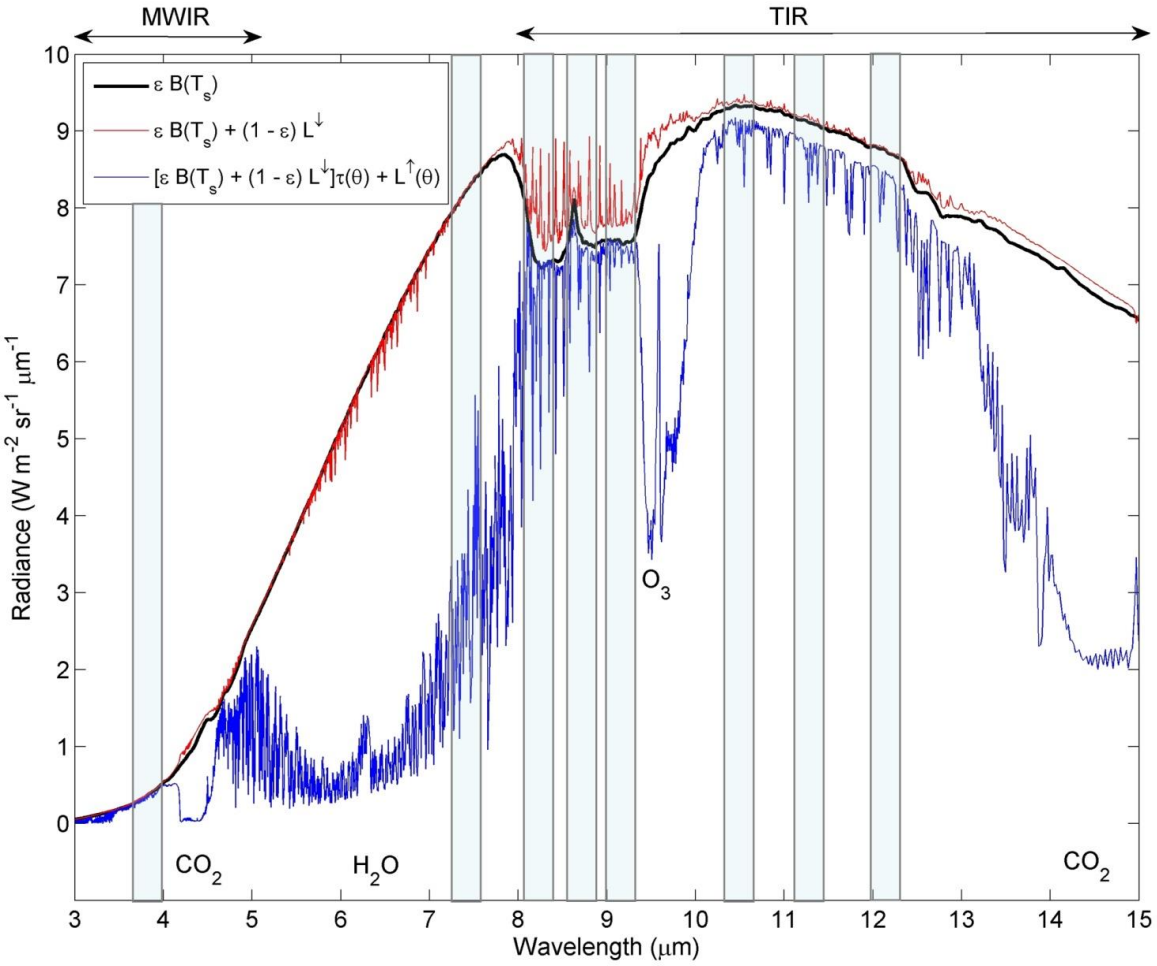

Figure 4. Radiance simulations of the surface-emitted radiance, surface-emitted and reflected radiance, and at-sensor radiance using the MODTRAN 5.2 radiative transfer code, US Standard Atmosphere, quartz emissivity spectrum, surface temperature = 300K, and viewing angle set to nadir. Vertical bars show placements of the HyspIRI MWIR and TIR bands.

Equation (1) gives the at-sensor radiance for a single wavelength, λ, while the measurement from a sensor is typically measured over a range of wavelengths, or band. The at-sensor radiance for a

discrete band, i, is obtained by weighting and normalizing the at-sensor spectral radiance calculated by equation (1) with the sensor's spectral response function for each band, Sr_λ, as follows:

$$L_i(\theta) = \frac{\int Sr_\lambda(\mathrm{i}) \cdot L_\lambda(\theta) \cdot \mathrm{d}\lambda}{Sr_\lambda(\mathrm{i}) \cdot \mathrm{d}\lambda} \tag{3}$$

Using equations (1) and (2), the surface radiance for band i can be written as a combination of two terms: Earth-emitted radiance, and reflected downward irradiance from the sky and surroundings:

$$L_{s,i} = \epsilon_i B_i(T_s) + (1-\epsilon_i)L_i^{\downarrow} = \frac{L_i(\theta) - L_i^{\uparrow}(\theta)}{\tau_i(\theta)} \tag{4}$$

The atmospheric parameters, $L_\lambda^{\downarrow}$, $\tau_\lambda(\theta)$, $L_\lambda^{\uparrow}(\theta)$, are estimated with a radiative transfer model such as MODTRAN (Kneizys et al. 1996) using input atmospheric fields of air temperature, relative humidity, and geopotential height.

The emissivity of an isothermal, homogeneous emitter is defined as the ratio of the actual emitted radiance to the radiance emitted from a black body at the same thermodynamic temperature (Norman and Becker 1995), $\epsilon_\lambda = R_\lambda/B_\lambda$. The emissivity is an intrinsic property of the Earth's surface and is an independent measurement of the surface temperature, which varies with irradiance and local atmospheric conditions. The emissivity of most natural Earth surfaces for the TIR wavelength ranges between 8 and 12 μm and, for a sensor with spatial scales <100 m, varies from ~0.7 to close to 1.0. Narrowband emissivities less than 0.85 are typical for most desert and semi-arid areas due to the strong quartz absorption feature (reststrahlen band) between the 8- and 9.5-μm range, whereas the emissivity of vegetation, water, and ice cover are generally greater than 0.95 and spectrally flat in the 8–12-μm range.

3.2 Temperature and Emissivity Separation Approaches

The radiance in the TIR atmospheric window (8–13 μm) is dependent on the temperature and emissivity of the surface being observed. Even if the atmospheric properties (water vapor and air temperature) are well known and can be removed from equation (1), the problem of retrieving surface temperature and emissivity from multispectral measurements is still a non-deterministic process. This is because the total number of measurements available (N bands) is always less than the number of variables to be solved for (emissivity in N bands and one surface temperature). Therefore, no retrieval will ever do a perfect job of separation, with the consequence that errors in temperature and emissivity

may co-vary. If the surface can be approximated as Lambertian (isotropic) and the emissivity is assigned *a priori* from a land cover classification, then the problem becomes deterministic with only the surface temperature being the unknown variable. Examples of such cases would be over ocean, ice, or densely vegetated scenes where the emissivity is known and spectrally flat in all bands. Another deterministic approach is the single-band inversion approach. If the atmospheric parameters are known in equation (1), then the temperature can also be solved for using a single band, usually in the clearest region of the window (~11 μm). Deterministic approaches are usually employed with sensors that have two or three bands in the TIR region, while non-deterministic approaches are applied to multispectral sensors so that spectral variations in the retrieved emissivity can be related to surface composition and cover, in addition to retrieving the surface temperature. For HyTES, a non-deterministic approach will be used, as spectral emissivity will need to be determined physically, along with temperature, in order to help answer the science questions outlined previously in section 3.

3.2.1 Deterministic Approaches

3.2.1.1 Split-window Algorithms

The most common deterministic approach can be employed without having to explicitly solve the radiative transfer equation. Two or more bands are employed in the window region (typically 10.5–12 μm), and atmospheric effects are compensated for by the differential absorption characteristics from the two bands. This approach is used with much success over oceans to compute the SST (Brown and Minnett 1999), as the emissivity of water is well known (Masuda et al. 1988). Variations of this method over land include the split-window (SW) approach (Coll and Caselles 1997; Prata 1994; Price 1984; Wan and Dozier 1996; Yu et al. 2008), the multichannel algorithm (Deschamps and Phulpin 1980), and the dual-angle algorithm (Barton et al. 1989). Over land, the assumption is that emissivities in the split-window bands being used are stable and well known and can be assigned using a land cover classification map (Snyder et al. 1998). However, this assumption introduces large errors over barren surfaces where much larger variations in emissivity are found due to the presence of large amounts of exposed rock or soil often with abundant silicates (Hulley and Hook 2009a). Land cover classification maps typically use VNIR data for assignment of various classes. This method may work for most vegetation types and over water surfaces but, because VNIR reflectances correspond predominately to Fe oxides and OH^- and not to the Si-O bond over barren areas, there is little or no correlation with silicate mineralogy features in thermal infrared data. This is why, in most classification maps, only one bare land class is specified (barren). This type of approach will not be used for the HyTES standard algorithm for the following reasons:

1. One of the goals of HyTES TIR science is to retrieve the spectral emissivity of geologic surfaces for compositional analysis. Classification does not produce this type of product.
2. The emissivity of the land surface is in general heterogeneous and is dependent on many factors including surface soil moisture, vegetation cover changes, and surface compositional changes, which are not characterized by classification maps.
3. Split-window algorithms are inherently very sensitive to measurement noise between bands.
4. Classification leads to sharp discontinuities and contours in the data between different class types. This violates one of the goals of HyTES in producing seamless images.
5. Temperature inaccuracies are difficult to quantify over geologic surfaces where constant emissivities are assigned.

3.2.1.2 Single-band Inversion

If the atmosphere is known, along with an estimate of the emissivity, then equation (1) can be inverted to retrieve the surface temperature using one band. Theoretically, any band used should retrieve the same temperature, but uncertainties in the atmospheric correction will result in subtle differences as different bands have stronger atmospheric absorption features than others which may be imperfectly corrected for atmospheric absorption. For example, a band near 8 μm will have larger dependence on water vapor, while the 9–10-μm region will be more susceptible to ozone absorption. Jimenez-Munoz and Sobrino (2010) applied this method to ASTER data by using atmospheric functions (AFs) to account for atmospheric effects. The AFs can be computed by the radiative transfer equation or empirically given the total water vapor content. The clearest ASTER band (13 or 14) was used to retrieve the temperature, with the emissivity determined using an NDVI fractional vegetation cover approach. A similar procedure has been proposed to retrieve temperatures from the Landsat TIR band 6 on ETM+ and TM sensors (Li et al. 2004). The single-band inversion method will not be used for HyTES for the following reasons:

1. One of the goals for HyTES science will be to retrieve the spectral emissivity of geologic surfaces for compositional analysis. This will not be possible with the single-band approach, which assigns emissivity based on land cover type and vegetation fraction.
2. Estimating emissivity from NDVI-derived vegetation cover fraction over arid and semi-arid regions will introduce errors in the LST because NDVI is responsive only to chlorophyll active vegetation, and does not correlate well with senescent vegetation (e.g., shrublands).

3. Only one-band emissivity is solved for the single-band inversion approach. HyTES will be a multispectral retrieval approach.

3.2.2 Non-deterministic Approaches

In non-deterministic approaches, the temperature and emissivity is solved using an additional constraint or extra degree of freedom that is independent of the data source. These types of solutions are also rarely perfect because the additional constraint will always introduce an additional level of uncertainty, however, they work well over all surfaces (including arid and semi arid) and can automatically account for changes in the surface e.g. due to fire or moisture. First, we introduce two well-known approaches, the day/night and TISI algorithms, followed by an examination of the algorithms and methods that led up to establishment of the TES algorithm.

3.2.2.1 Day/Night Algorithm

The constraint in the day/night algorithm capitalizes on the fact that the emissivity is an intrinsic property of the surface and should not change from day- to nighttime observations. The day/night algorithm is currently used to retrieve temperature/emissivity from MODIS data in the MOD11B1 product (Wan and Li 1997). The method relies on two measurements (day and night), and the theory is as follows: Two observations in N bands produces 2N observations, with the unknown variables being N-band emissivities, a day- and nighttime surface temperature, four atmospheric variables (day and night air temperature and water vapor), and an anisotropic factor, giving N + 7 variables. In order to make the problem deterministic, the following conditions must be met: $2N \geq N+7$, or $N \geq 7$. For the MODIS algorithm, this can be satisfied by using bands 20, 22, 23, 29, 31–33. Although this method is theoretically sound, the retrieval is complicated by the fact that two clear, independent observations are needed (preferably close in time) and the pixels from day and night should be perfectly co-registered. Errors may be introduced when the emissivity changes from day to night observation (e.g., due to condensation or dew), and from undetected nighttime cloud. In addition, the method relies on very precise co-registration between the day- and nighttime pixel.

3.2.2.2 Temperature Emissivity Separation Approaches

During research activities leading up to the ASTER mission, the ASTER Temperature Emissivity Working Group (TEWG) was established in order to examine the performance of existing non-deterministic algorithms and select one suitable for retrieving the most accurate temperature and/or emissivity over the entire range of terrestrial surfaces. This lead to development of the TES algorithm, which ended up being a hybrid algorithm that capitalized on the strengths of previous

algorithms. In Gillespie et al. (1999), ten inversion algorithms were outlined and tested, leading up to development of TES. For all ten algorithms, an independent atmospheric correction was necessary. The ten algorithms were as follows:

1. Alpha-derived emissivity (ADE) method
2. Classification method
3. Day-Night measurement
4. Emissivity bounds method
5. Graybody emissivity method
6. Mean-MMD method (MMD)
7. Model emissivity method
8. Normalized emissivity method (NEM)
9. Ratio Algorithm
10. Split-window algorithm

In this document, we will briefly discuss a few of the algorithms but will not expand upon any of them in great detail. The day-night measurement (3), classification (2), and split-window (10) algorithms have already been discussed in section 4.2.1. A detailed description of all ten algorithms is available in Gillespie et al. (1999). The various constraints proposed in these algorithms either determine spectral shape but not temperature, use multiple observations (day and night), assume a value for emissivity and calculate temperature, assume a spectral shape, or assume a relationship between spectral shape and minimum emissivity.

The normalized emissivity method (NEM) removes the downwelling sky irradiance component by assuming an ϵ_{max} of 0.99. Temperature is then estimated by inverting the Planck function and a new emissivity found. This process is repeated until successive changes in the estimated surface radiances are small. This method in itself was not found to be suitable for ASTER because temperature inaccuracies tended to be high (>3 K) and the emissivities had incorrect spectral shapes. Other approaches have used a model to estimate emissivity at one wavelength (Lyon 1965) or required that the emissivity be the same at two wavelengths (Barducci and Pippi 1996). This introduces problems for multispectral data with more than 5 bands, e.g., ASTER or HyspIRI.

The ADE method (Hook et al. 1992; Kealy et al. 1990; Kealy and Hook 1993) is based on the alpha residual method that preserves emissivity spectral shape but not amplitude or temperature. The

constraint introduced uses an empirical relationship between spectral contrast and average emissivity to restore the amplitude of the alpha-residual spectrum and to compute temperature. The average emissivity was used in the relationship to minimize band-to-band calibration errors. The TEWG used this key feature of the ADE method in TES, although the minimum emissivity instead of average emissivity was used in the empirical relationship (Matsunaga 1994). The ADE itself was not fully employed for two primary reasons as discussed in Gillespie et al. (1999): 1) ADE uses Wien's approximation, $\exp(x) - 1 = \exp(x)$, which introduces a noticeable "tilt" in the residual spectra that gets transferred to the final emissivity spectra; and 2) This issue was easily fixed in the hybrid version of TES.

Lastly, the temperature-independent spectral indices (TISI) approach (Becker and Li 1990) computes relative emissivities from power-scaled brightness temperatures. TISI, however, is band-dependent and only recovers spectral shape; furthermore, the values are non-unique. To retrieve actual emissivities, additional information or assumptions are needed. Other algorithms, which only retrieve spectral shape, are the thermal log and alpha residual approach (Hook et al. 1992) and spectral emissivity ratios (Watson 1992; Watson et al. 1990). Neither of these were considered because they do not recover temperature or actual emissivity values.

4 Atmospheric Correction

The spectral radiance in equation 1 will include atmospheric emission, scattering, and absorption by the Earth's atmospheric constituents. In order to isolate the land-leaving surface radiance and estimate the surface temperature and emissivity, these atmospheric effects need to be removed from the observation. For on-plume pixel observations, the atmospheric compensation isolates the land-leaving radiance contribution in addition to reducing the wavelength dependence of the plume strength (difference between radiance emitted by plume and ground). Typically the success of complete atmospheric correction is dependent upon accurate characterization of the atmospheric state input into a radiative transfer model for estimating atmospheric transmittance, path radiance, and sky irradiance. Independent atmospheric profiles of temperature, water vapor, and other gas constituents (e.g., ozone) are required as input to the radiative transfer model. Only once the residual effects of the atmosphere have been removed from the observed radiance is it possible to infer surface compositional features, and estimate the surface temperature.

The radiative transfer model method has been used successfully in the past to account for atmospheric effects from narrow-band thermal infrared sensors such as ASTER and MODIS on NASA Terra platform, which have well defined spectral response functions situated in atmospheric windows of the thermal infrared domain (8-12 micron). The accuracy of this approach relies mostly on the representativeness of the atmospheric profile data for the observation of interest, both in space and time, and particularly the contribution of the water vapor effects. For hyperspectral data, for example HyTES from 7.6-12 micron, atmospheric correction is more challenging because bands are situated in atmospheric absorption features and complications arise when the output model data from MODTRAN are not accurately spectrally registered to the observed data. This could occur if the sensors spectral responses functions are not precisely defined in addition to band-to-band registration issues. In these cases even small misregistrations near strong absorption lines will amplify instead of reduce the effects of atmospheric absorption for the surface radiance spectrum. An example of this problem is illustrated in Figures 5 and 6.

4.1.1 ISAC Approach

To circumvent these issues, an in-scene atmospheric correction (ISAC) approach was developed for Aerospace Corporation for the SEBASS hyperspectral sensor (Young et al. 2002). The big advantage of the ISAC method is that atmospheric correction is accomplished using the

hyperspectral data itself without the need for external atmospheric profiles. In addition the issue of spectral band misregistrations is eliminated. However there are some limitations to this

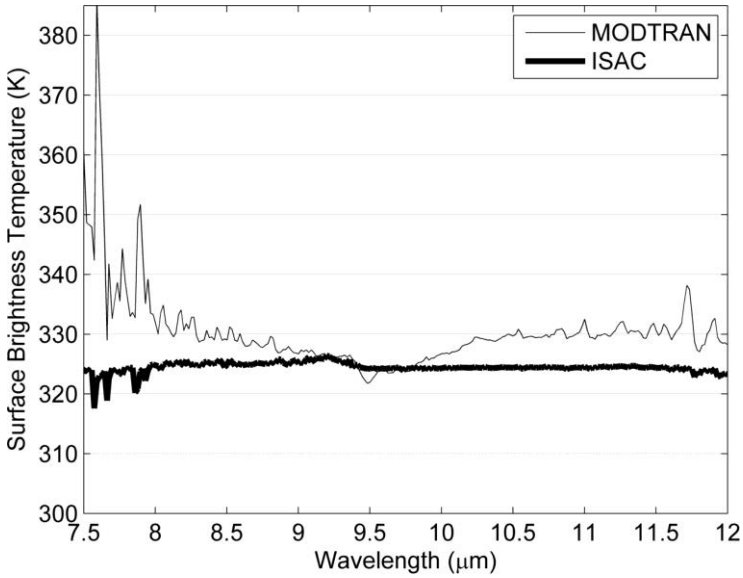

Figure 5. An example of surface brightness temperature spectra from HyTES after atmospheric correction using the RTM approach with MODTRAN (gray line), and the ISAC approach (black line). With a successful atmospheric correction we expect a nearly constant temperature across all bands, which is achievable with the ISAC approach but not with MODTRAN below 8 µm and above 11.5 µm because of misregistrations between HyTES data and MODTRAN.

approach that limits its usefulness for certain conditions and surface types. The ISAC method makes two primary assumptions, 1) the atmosphere is uniform over the data scene and 2) pixels with near-blackbody characteristics that have emissivities close to 1 (e.g. vegetation, water, some rocks and soils) exist within the scene that have variable temperatures, preferably over a large range. The location of the blackbody pixels is not required for this correction algorithm. Using the blackbody assumption, $\epsilon_\lambda \sim 1$, the observed radiance in (1) can be written as a linear function with independent variable, $B_\lambda(T_s)$, with slope τ_λ^{atm} and y-intercept $L_\lambda^{\downarrow}$ as follows:

$$L_\lambda = \left[B_\lambda(T_s)\tau_\lambda^{atm} + L_\lambda^{\downarrow}\right] \quad (5)$$

Theoretically, the atmospheric parameters τ_λ^{atm} and $L_\lambda^{\downarrow}$ can then be found by simple linear regression by plotting L_λ^{off} vs $B_\lambda(T_s)$ for all pixels on a scene for a given wavelength. However, in general $B_\lambda(T_s)$ is unknown because we don't know the surface temperature, and we also don't know which pixels on the scene meet the $\epsilon_\lambda \sim 1$ criteria (i.e. graybody pixels).

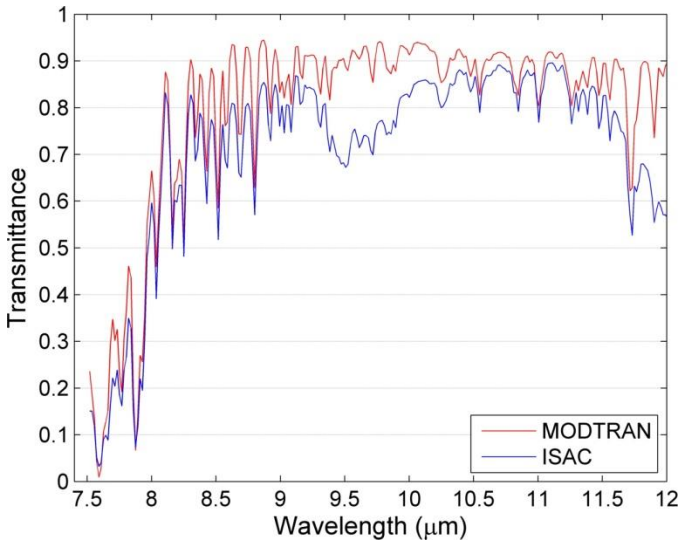

Figure 6. Differences between MODTRAN and ISAC transmittance estimates for HyTES data. Note while the absorption features are similar, there are some large differences in absolute magnitude due to misregistration of the spectral response functions in MODTRAN, and calibration issues above 11.5 micron. Using the HyTES data itself for the correction (ISAC) eliminates these issue as discussed in the text.

The approach suggested by Young et al. 2002 to find graybody pixels on a scene is to examine each pixel's spectra to find the wavelength at which the maximum brightness temperature occurs (usually $\epsilon_\lambda \sim 1$). The spectral channel that was chosen to be the maximum the most times is then considered to be the 'reference' wavelength, and only those pixels with the reference wavelength as maximum are chosen as graybody pixels and used in the scatterplot. Young et al. 2002 termed this the "most hits" method of reference channel selection. This wavelength, λref, is then used as the reference wavelength and only pixels that have their maximum brightest temperature at this wavelength are used to calculate the atmospheric parameters. An example of this application is shown in Figure 7 which plots the HyTES radiances versus the estimated blackbody radiances. The slope and y-intercept of a fit to the top-most data points (red line) in the plot yields the transmittance and path radiance in equation 5.

In our experience with HyTES data, however, we discovered that this approach did not work consistently for all scenes that contained a mix of bare and graybody surface types. For example, many pixels of different types of soils in agricultural environments with emissivities <0.95 were also included using the 'most hits' method described above, and verified by using emissivity information from the ASTER Global Emissivity Database (ASTER GED) (Hulley et al. 2015). These non-graybody pixels violate the assumptions of equation (5) and lead to errors

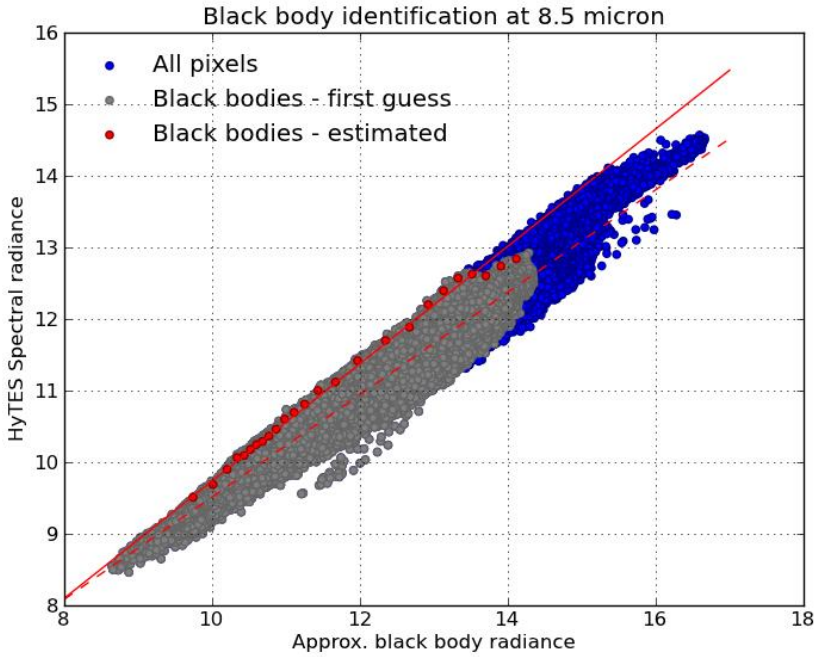

Figure 7. Example of application of the ISAC method with HyTES data to identify blackbody pixels and estimate the slope (transmittance) and y-intercept (path radiance) from equation 5. A fit through the top-most data points in the distribution of data is required to isolate the near-blackbody pixels.

in the fitting procedure. As an alternative approach, we calculated the radiance spectral variance for each pixel and only those pixels with low variance (e.g. less than 8 W/m^2) were assumed to be graybody pixels suitable for use in the fitting procedure. The spectral variance approach is a good assumption for low altitude flights (1 km AGL) in which observed radiance is still representative of surface spectral features, and also because graybody surfaces such as vegetation, snow, ice, and water have very low spectral variance in emissivity in the 8-12 micron range.

In the next step and demonstrated in Figure 7, the observed radiance is plotted against the blackbody radiance calculated from the brightness temperature at the reference wavelength chosen in the previous step, i.e. $B_\lambda\left(T_{\lambda ref}\right)$. A line fitting procedure is then used to fit the highest points in the plotted data which represent the condition $\epsilon_\lambda \sim 1$. Fitting a line through the center of the data using traditional least squares will not work here, but instead a statistical method based on a probability distribution model is used to fit a line through the top points. More details of the line fitting procedure can be found in Young et al. 2002. The atmospheric parameters τ_λ^{atm} and $L_\lambda^{\uparrow}$ are then estimated as the slope and intercept of the regression line through the top of the data cluster as shown in Figure 7. Examples of HyTES atmospheric path radiance and transmittance spectra derived from ISAC are

shown in Figure 8 for a flight altitude of 3-km AGL. Absorption and emission features from water vapor appear as spikes in the path radiance and depressions in the transmittance.

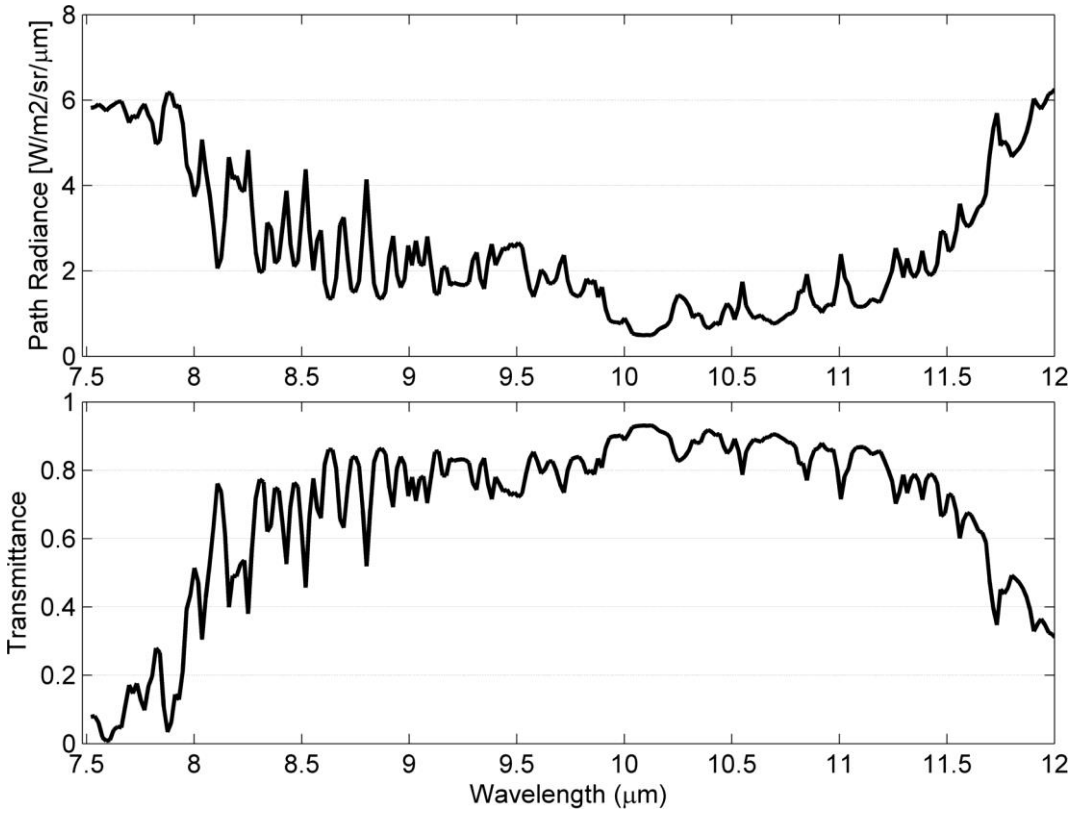

Figure 8. HyTES path radiance (top) and transmittance (bottom) spectra estimated from the ISAC method for a flight at 3-km AGL. Absorption and emission features from water vapor appear as spikes in the path radiance and corresponding troughs in the transmittance spectra.

4.1.2 ISAC Scaling

The next step is to scale these atmospheric spectra to the true atmospheric conditions on the scene. Because of some assumptions made in their derivation (maximum brightness temperature may not be true surface temperature), they may not conform to what is expected of true conditions. For example there may be transmittances greater than 1 or less than zero, even although the spectral structure of the atmospheric parameters are correct, and consistent with the data being used. To scale the parameters back into physical ranges, we use an independent source of atmospheric compensation and adjust to match for one channel in a least squares sense. For HyTES we have used the MODTRAN radiative transfer model combined with NCEP atmospheric profiles of water vapor and air temperature to derive the path radiance and transmittance and convolved to the HyTES spectral response functions. The scaling procedure is detailed in Young et al. and will not be shown here, however examples of the

differences between the ISAC parameters and MODTRAN estimates are shown in Figure 6 for the transmittance.

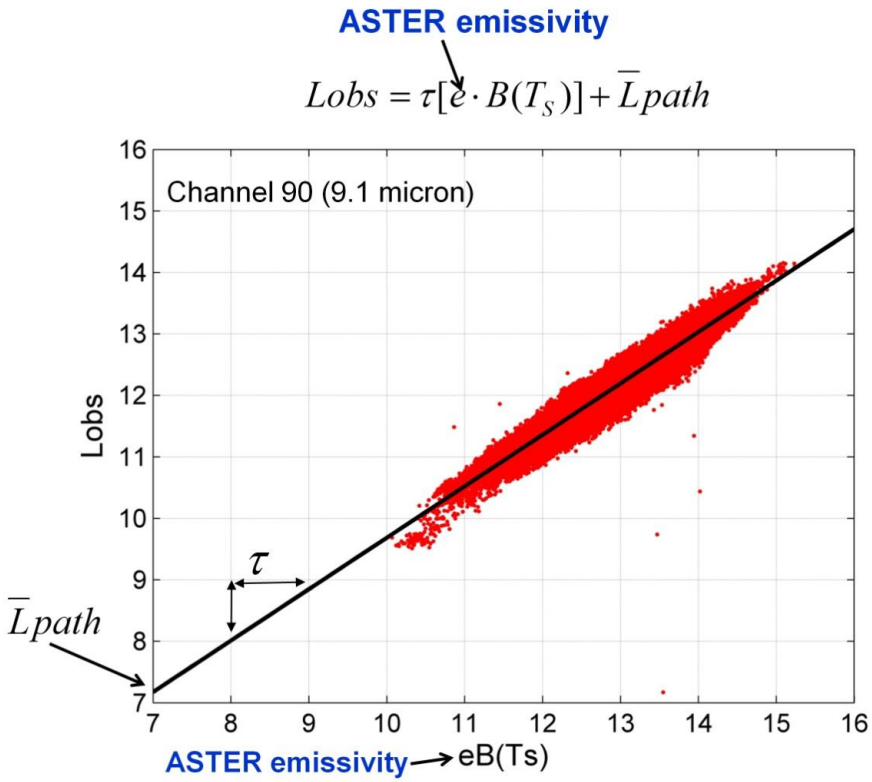

Figure 9. Example of ISAC-ASTER correction approach for Algodones dunes data (all bare pixels). In this approach emissivity data from the ASTER GED is used to estimate the surface emitted radiance (x-axis) in this case for channel 90 (9.1 micron). The ASTER GED data was convolved to the HyTES spectral response at this wavelength. For this approach, the fitting procedure to the top-most data points is not necessary, and a simple linear regression fit through the data is sufficient to estimate the transmittance (slope) and path radiance (y-intercept).

4.1.3 ISAC for bare surfaces: ISAC-ASTER approach

A large number of the HyTES target sites including those over a few key methane hotspots (e.g. Kern River Oil Field) were flown over bare regions containing very few graybody pixels (e.g. vegetation, water) and an alternative ISAC approach had to be developed that was independent of the inherent blackbody pixel assumption. In this approach, termed the 'ISAC-ASTER' method, emissivity information from the ASTER GED 5 TIR bands from 8-12 µm were used directly in the ISAC fitting procedure instead of relying on the blackbody assumption. An example of this approach for a line over the Algodones dunes data (all bare pixels) is shown in Figure 9. Here ASTER GED emissivity information was used to estimate the surface emitted radiance (x-axis) in this case for channel 90 (9.1 micron). For this approach, the fitting procedure to the top-most data points is not necessary, and a

simple linear regression fit through the data is sufficient to estimate the transmittance (slope) and path radiance (y-intercept).

ASTER GED emissivities at 100 m spatial resolution are first geolocated and interpolated onto the HyTES scene and then a Principal component (PC) regression approach (Borbas et al. 2007) is used to extend the 5 ASTER band emissivities to the 256 HyTES bands from 7.4-12 µm (Hulley and Guillevic 2015; Hulley et al. 2014). Figure 10 shows an example of HyTES observed and estimated surface radiance using the ISAC-ASTER version for data acquired over the Algodones Dunes, CA during July 2014 at 3-km AGL. The spectral shape of the quartz doublet between 8.3-9 µm is clearly evident after atmospheric correction leaving only residual lines from the reflected downwelling radiance component. Validation of retrieved emissivity using the Temperature Emissivity Separation (TES) algorithm from these data match lab spectra of sand samples collected at the Algodones dunes to within <2% in the 8-12 µm window bands as shown in Figure 14 (Hulley et al. 2014).

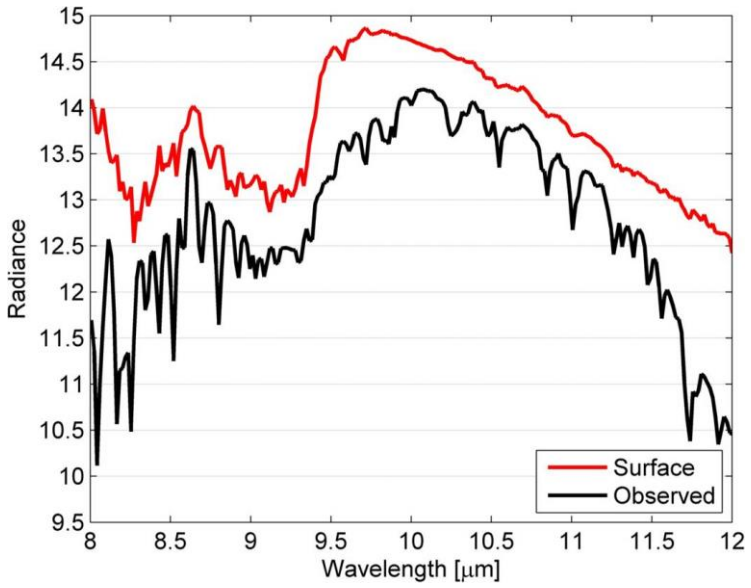

Figure 10. HyTES observed (black) and surface (red) radiance in W/m2/sr/µm for data acquired over the Algodones Dunes, CA at 3-km AGL. The surface radiance was estimated using the ISAC-ASTER correction described in the text. The spectral shape of the quartz doublet between 8.3-9 µm is clearly evident after atmospheric correction.

4.1.4 Estimation of downwelling sky irradiance

To remove the independence on using a RT model to estimate the downwelling sky irradiance, $L_{\lambda}^{\downarrow}$, in eq. (1), $L_{\lambda}^{\downarrow}$ can be can be modeled as a function of path radiance, transmittance, and view angle of the sensor. Radiative transfer runs with MODTRAN are first computed for a range of atmospheric

conditions using globally representative radiosonde profiles and surface temperatures. To simulate the downward sky irradiance in MODTRAN, the sensor target is placed a few meters above the surface, with surface emission set to zero, and view angle set at desired range of angles of given sensor. Output path and downwelling sky radiances can then be computed and tabulated by sensor wavelength and view angle. For HyTES, a pushbroom instrument with IFOV if 1.7 mrad, we can assume view angles of near zero for flights below 3 km in altitude. Figure 11 shows an example of sky irradiance plotted versus path radiance for an altitude of 20km (ER2 flights) using MODTRAN simulations. From the quadtratic fit its clear that sky irradiance can be modeled from the path radiance with small error.

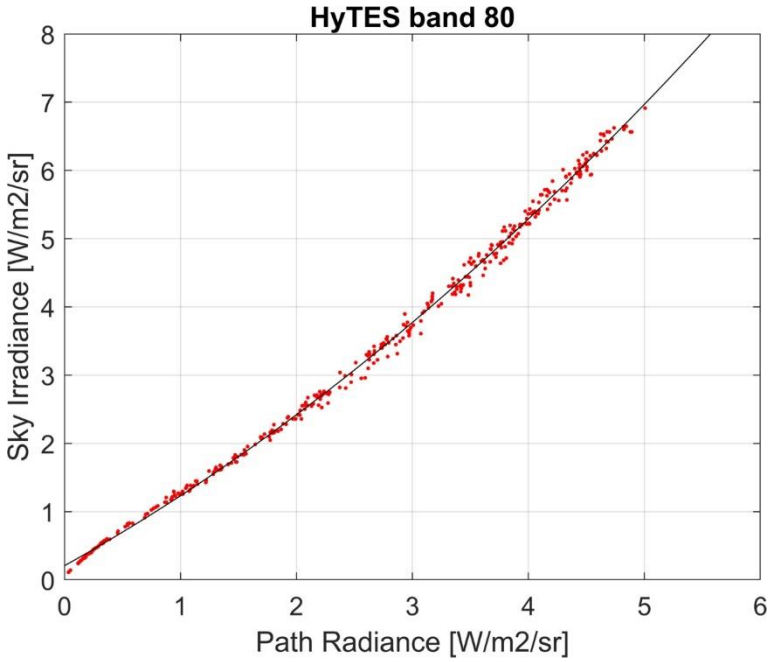

Figure 11. HyTES sky irradiance versus path radiance (W/m2/sr/µm) for band 80 (8.9 µm) from MODTRAN simulations using globally representative radiosonde profiles from SeeBor.

The downward sky irradiance can be modeled as a non-linear function of path radiance at nadir view (Tonooka 2001):

$$L_\lambda^\downarrow = a_i + b_i \cdot L_\lambda^\uparrow + c_i L_\lambda^{\uparrow 2} \quad (6)$$

where a_i, b_i, and c_i are regression coefficients and need to be computed for each altitude that that instrument is flown. The reflected sky irradiance term is generally smaller in magnitude than the surface-emitted radiance, but needs to be taken into account, particularly on humid days over bare surfaces when the total atmospheric water vapor content and surface reflectances are high.

5 Temperature Emissivity Separation (TES) Algorithm

The final TES algorithm proposed by the ASTER TEWG combined some core features from previous algorithms and, at the same time, improved on them. TES combines the NEM, the ratio, and the minimum-maximum difference (MMD) algorithm to retrieve temperature and a full emissivity spectrum. The NEM algorithm is used to estimate temperature and iteratively remove the sky irradiance, from which an emissivity spectrum is calculated, and then ratioed to their mean value in the ratio algorithm. At this point, only the shape of the emissivity spectrum is preserved, but not the amplitude. In order to compute an accurate temperature, the correct amplitude is then found by relating the minimum emissivity to the spectral contrast (MMD). Once the correct emissivities are found, a final temperature can be calculated with the maximum emissivity value. Additional improvements involve a refinement of ϵ_{max} in the NEM module and refining the correction for sky irradiance using the ε_{min}-MMD final emissivity and temperature values. Finally, a quality assurance (QA) data image is produced that partly depends on outputs from TES such as convergence, final ϵ_{max}, atmospheric humidity, and proximity to clouds. More detailed discussion of QA is included later in this document.

Numerical modeling studies performed by the ASTER TEWG showed that TES can recover temperatures to within 1.5 K and emissivities to within 0.015 over most scenes, assuming well calibrated, accurate radiometric measurements (Gillespie et al. 1998).

5.1 Data Inputs

Inputs to the TES algorithm are the surface radiance, $L_{s,i}$, given by equation (4) (at-sensor radiance corrected for transmittance and path radiance), and downwelling sky irradiance term, $L_{\lambda}^{\downarrow}$, which for HyTES are computed using the ISAC approach. Both the surface radiance and sky irradiance will be output as a separate product. The surface radiance is primarily used as a diagnostic tool for monitoring changes in Earth's surface composition.

5.2 TES Limitations

As with any retrieval algorithm, limitations exist that depend on measurement accuracy, model errors, and incomplete characterization of atmospheric effects. The largest source of inaccuracy currently for ASTER data is the residual effect of incomplete atmospheric correction. Measurement accuracy and precision contribute to less of a degree. This problem is compounded for graybodies, which have low spectral contrast and are therefore more prone to errors in "apparent" MMD, which is

overestimated due to residual sensor noise and incomplete atmospheric correction. A threshold classifier was introduced by the TEWG to partly solve this problem over graybody surfaces. Instead of using the calibration curve to estimate ε_{min} from MMD, a value of ε_{min}= 0.983 was automatically assigned when the spectral contrast or MMD in emissivity was smaller than 0.03 for graybody surfaces (e.g., water, vegetation). However, this caused artificial step discontinuities in emissivity between vegetated and arid areas.

At the request of users, two parameter changes were made to the ASTER TES algorithm on August 1, 2007, first described in Gustafson et al. (2006). Firstly, the threshold classifier was removed as it caused contours and artificial boundaries in the images that users could not tolerate in their analysis. The consequence of removing the threshold classifier was a smoother appearance for all images but at the cost of TES underestimating the emissivity of graybody scenes, such as water by up to 3% and vegetation by up to 2% (Hulley et al. 2008). The second parameter change removed the iterative correction for reflected downwelling radiation, which also frequently failed due to inaccurate atmospheric corrections (Gustafson et al. 2006). Using only the first iteration resulted in improved spectral shape and performance of TES.

5.3 TES Processing Flow

Figure 12 shows the processing flow diagram for the generation of HyTES data from raw uncalibrated radiances, to L1B radiometrically calibrated and orthorectified radiances, to L2 land surface temperature and emissivity and L3 gas detection products. The L1B, L2 and L3 products all include Google Earth kmz files and corresponding metadata. Figure 13 shows a more detailed processing flow of the TES algorithm itself. Each of the steps will be presented in sufficient detail in the following section, allowing users to regenerate the code. TES uses input image data of surface radiance, $L_{s,i}$, and sky irradiance, $L_{\lambda}^{\downarrow}$, to solve the TIR radiative transfer equation.

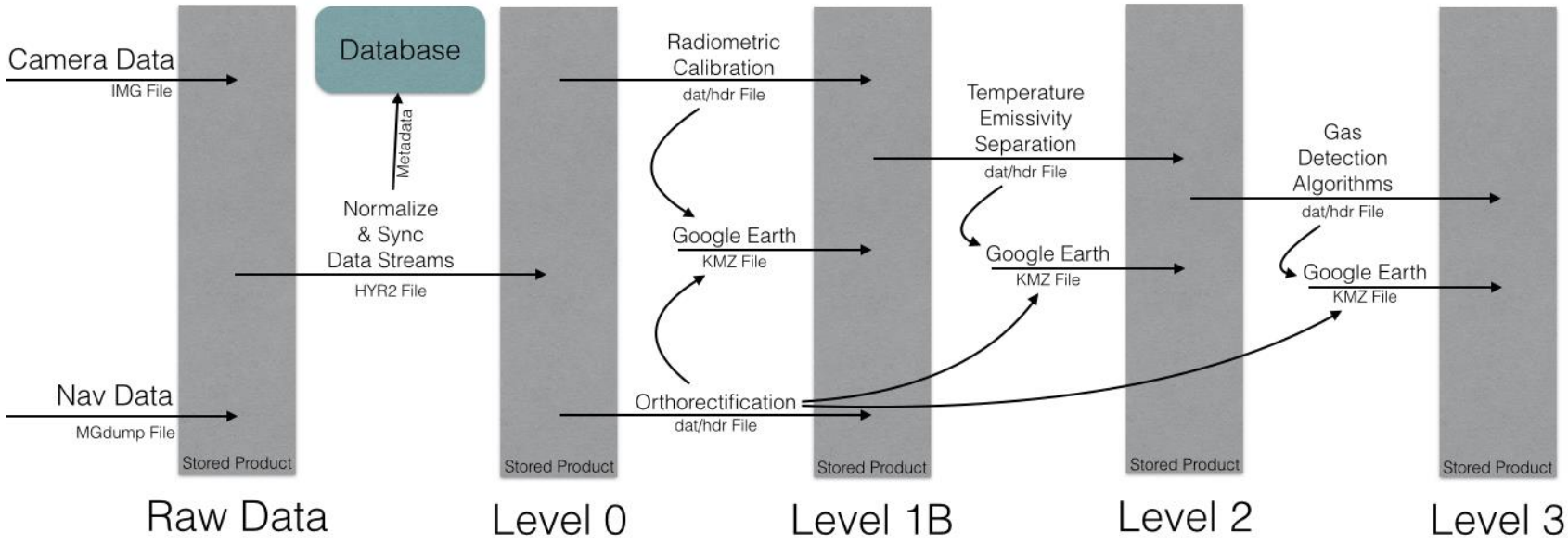

Figure 12. Flow diagram showing all steps in the processing of HyTES data from raw uncalibrated radiances, to L1B radiometrically calibrated and orthorectified radiances, to L2 land surface temperature and emissivity and L3 gas detection products. The L1B, L2 and L3 products all include Google Earth kmz files and corresponding metadata.

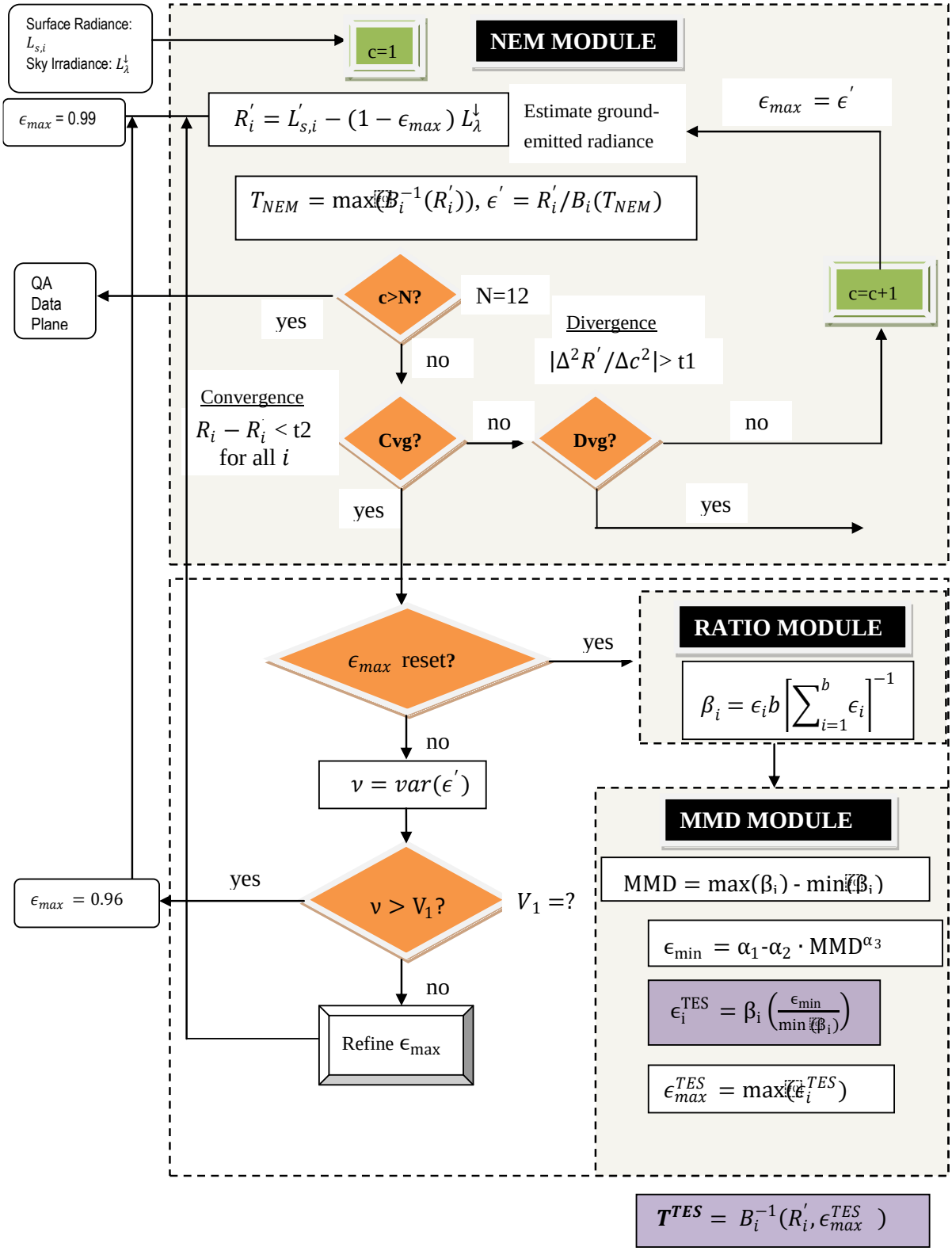

Figure 13. Flow diagram of the TES algorithm in its entirety, including the NEM, RATIO and MMD modules. Details are included in the text, including information about the refinement of ϵ_{max}.

5.4 NEM Module

The normalized emissivity method (NEM) builds upon the model emissivity algorithm (Lyon 1965) by allowing the initial ϵ_{max} value to be consistent for all wavelengths. The role of NEM is to compute the surface kinetic temperature, T, and a correct shape for the emissivity spectrum. An initial value of 0.99 is set for ϵ_{max}, which is typical for most vegetated surfaces, snow, and water. For geologic materials such as rocks and sand, ϵ_{max} values are set lower than this, typically 0.96, and this value remains fixed. For all other surface types, a modification to the original NEM allows for optimization of ϵ_{max} using an empirically based process. For the majority of materials in the ASTER spectral library, a typical range for ϵ_{max} is $0.94<\epsilon_{max}<1.0$. Therefore, for a material at 300 K, the maximum errors that NEM temperatures should have are ~±1.5 K, assuming the reflected sky irradiance has been estimated correctly.

5.5 Subtracting Downwelling Sky Irradiance

Generally the effects of sky irradiance are small with typical corrections of <1 K (Gillespie et al. 1998). However, the contribution becomes larger for pixels with low emissivity
(high reflectance) or in humid conditions when the sky is warmer than the surface. Over graybody surfaces (water and vegetation), the effects are small because of their low reflectivity in all bands. The first step of the NEM module is to estimate ground-emitted radiance, which is found by subtracting the reflected sky irradiance from the surface radiance term:

$$R_i = L'_{s,i} - (1 - \epsilon_{max})\, L^{\downarrow}_{\lambda} \tag{7}$$

The NEM temperature, which we call T_{NEM}, is then estimated by inverting the Planck function for each band using ϵ_{max} and the ground-emitted radiance and then taking the maximum of those temperatures. The maximum temperature will most likely be closest to the actual surface temperature in the presence of uncompensated atmospheric effects.

$$T_i = \frac{c_2}{\lambda_i}\left(ln\left(\frac{c_1\epsilon_{max}}{\pi R_i \lambda_i^5} + 1\right)\right)^{-1} \tag{8}$$

$$T_{NEM} = \max(T_i) \tag{9}$$

The NEM emissivity spectrum is then calculated as the ratio of emitted radiance to that of a blackbody with a temperature estimated by T_{NEM}:

$$\epsilon'_i = \frac{R_i}{B_i(T_{NEM})} \tag{10}$$

The new emissivity spectrum is then used to re-calculate $R_i' = L'_{s,i} - (1 - \epsilon_i') L_\lambda^\downarrow$, and the process is repeated until convergence, which is determined if the change in R_i between steps is less than a set threshold, t_2, which is set as the radiance equivalent to NEΔT of the sensor. The process is stopped if the number of iterations exceeds a limit N, set to 12. Execution of the NEM module is also aborted if the slope of R_i versus iteration, c, increases such that $|\Delta^2 R'/\Delta c^2| > t_1$, where t_1 is also set to radiance equivalent of NEΔT for the sensor. In this case, correction is not possible, TES is aborted, and NEM values of ϵ_i and T_{NEM} are reported in the QA data plane, along with an error flag. TES is also aborted and an error flag recorded if, for any iteration, the values of ϵ_i fall out of reasonable limits, set to $0.5 < \epsilon_i < 1.0$. See Figure 13 for a detailed description of these steps.

5.6 Refinement of ϵ_{max}

First an initial guess of maximum emissivity is assumed, usually ϵ_{max} = 0.99 and subsequent refinement of ϵ_{max} is necessary to improve accuracy of T_{NEM}. The optimal value for ϵ_{max} minimizes the variance, ν, of the NEM calculated emissivities, ϵ_i. The optimization of ϵ_{max} is only useful for pixels with low emissivity contrast (near graybody surfaces) and therefore is only executed if the variance for ϵ_{max}= 0.99 is less than an empirically determined threshold (e.g., $V_1 = 1.7 \times 10^{-4}$ for ASTER) (Gillespie et al. 1998). If the variance is greater than V_1, then the pixel is assumed to predominately consist of either rock or soil. For this case, ϵ_{max} is reset to 0.96, which is a good first guess for most rocks and soils in the ASTER spectral library, which typically fall between the 0.94 and 0.99 range. If the first condition is met, and the pixel is a near-graybody, then values for ϵ_{max} of 0.92, 0.95, 0.97, and 0.99 are used to compute the variance for each corresponding NEM emissivity spectrum. A plot of variance ν versus each ϵ_{max} value results in an upward-facing parabola with the optimal ϵ_{max} value determined by the minimum of the parabola curve in the range $0.9 < \epsilon_{max} < 1.0$. This minimum is set to a new ϵ_{max}value, and the NEM module is executed again to compute a new T_{NEM}. Further tests are used to see if a reliable solution can be found for the refined ϵ_{max}. If the parabola is too flat, or too steep, then refinement is aborted and the original ϵ_{max} value is used. The steepness condition is met if the first derivative (slope of ν vs. ϵ_{max}) is greater than a set threshold (e.g., $V_2 = 1.0 \times 10^{-3}$) and the flatness conditions is met if the second derivative is less than a set threshold (e.g., $V_3 = 1.0 \times 10^{-3}$). Finally, if the minimum ϵ_{max} corresponds to a very low ν, then the spectrum is essentially flat (graybody) and the original ϵ_{max} = 0.99 is used. This condition is met if $\nu_{min} < V_4$ (e.g. $V_2 = 1.0 \times 10^{-4}$). These thresholds are determined empirically. Table 2 shows typical output from various stages of the TES algorithm for pixels representing three different surface types:

sand dunes, vegetated cropland, and semi-vegetated cropland for an ASTER scene on July 15, 2000, over the Imperial Valley, southeastern California. Note the different ϵ_{max} value for each of these surface types. The dune pixel was set to 0.96 due to large variance in emissivity; the fully vegetated pixel was set to 0.983, a typical value for a graybody; and ϵ_{max} for the semi-vegetated pixel needed to be optimized, resulting in a final value of 0.969.

Table 2. Output from various stages of the TES algorithm for three surface types; sand dunes, vegetated cropland, and semi-vegetated cropland for a HyTES scene over the Salton Sea region in southeastern California.

	Algodones Dunes	Cropland (vegetated)	Cropland (semi-vegetated)
ϵ_{max}	0.96	0.983	0.969
MMD	0.189	0.013	0.028
ϵ_{min}	0.793	0.967	0.944
T_{NEM}	337.06 K	305.92 K	319.75 K
T_{TES}	337.41 K	306.14 K	319.65 K

5.7 Ratio Module

In the ratio module, the NEM emissivities are ratioed to their average value to calculate a β_i spectrum as follows:

$$\beta_i = \frac{\epsilon_i}{\bar{\epsilon}} \tag{11}$$

Typical ranges for the β_i emissivities are $0.75 < \beta_i < 1.32$, given that typical emissivities range from 0.7 to 1.0. Errors in the β_i spectrum due to incorrect NEM temperatures are generally systematic.

5.8 MMD Module

In the minimum-maximum difference (MMD) module, the β_i emissivities are scaled to an actual emissivity spectrum using information from the spectral contrast or MMD of the β_i spectrum. The MMD can then be related to the minimum emissivity, ϵ_{min}, in the spectrum using an empirical relationship determined from lab measurements of a variety of different spectra, including rocks, soils, vegetation, water, and snow/ice. The relationship between MMD and ϵ_{min} is physically reasonable and is determined using a set of laboratory spectra in the ASTER spectral library v2.0 (Baldridge et al. 2009) and referred to as the calibration curve. The original ASTER regression coefficients were determined from a set of 86 laboratory reflectance spectra of rocks, soils, water, vegetation, and snow supplied by J.W. Salisbury from Johns Hopkins University. One question that needed to be answered was whether using a smaller or larger subset of this original set of spectra changed the results in any

manner. Establishing a reliable MMD vs. ϵ_{min} relationship with a subset of spectral representing all types of surfaces is a critical assumption for the calibration curve. This assumption was tested using various combinations and numbers of different spectra (e.g., Australian rocks, airborne data, and a subset of 31 spectra from Salisbury), and all yielded very similar results to the original 86 spectra.

For HyTES, the original 86 spectra were updated to include additional sand spectra used to validate the North American ASTER Land Surface Emissivity Database (NAALSED) (Hulley and Hook 2009b) and additional spectra for vegetation from the MODIS spectral library and ASTER spectral library v2.0, giving a total of 150 spectra. The data were convolved to the nominal HyTES bands and ϵ_{min} and β_i spectra calculated for each sample. The MMD for each spectra was then calculated from the β_i spectra and regressed to the ϵ_{min} values. The relationship follows a simple power law given by equation 12, with regression coefficients α_1= 0.9961, $\alpha_2 = 0.7929$, and $\alpha_3 = 0.8234$, and $R^2 = 0.987$. Figure 14 shows the power-law relationship between MMD and ϵ_{min} using the 150 lab spectra.

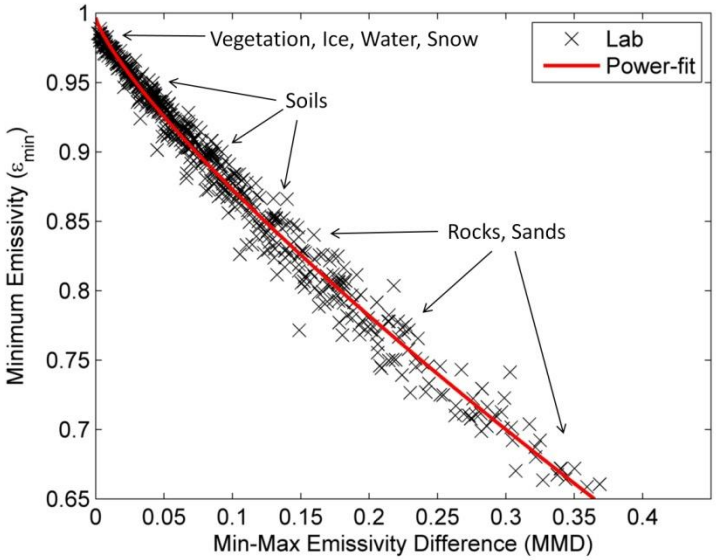

Figure 14. HyTES calibration curve of minimum emissivity vs. min-max difference (MMD). The lab data (crosses) are computed from 150 spectra consisting of a broad range of terrestrial materials.

From ϵ_{min}, the actual emissivity spectrum can be found by re-scaling the β_i spectrum. First, the MMD of the β_i spectrum is found by:

$$MMD = \max(\beta_i) - \min(\beta_i) \quad (12)$$

Then MMD can be related to ϵ_{min} using a power-law relationship:

$$\epsilon_{min} = \alpha_1 - \alpha_2 MMD^{\alpha_3}, \quad (13)$$

where α_j are coefficients that are obtained by regression using lab measurements. For the 202 HyTES window bands between 8 and 11.5 µm (shown in Figure 14), the values for the coefficients were calculated as α_1= 0.9961, $\alpha_2 = 0.7929$, and $\alpha_3 = 0.8234$. The TES emissivities are then calculated by re-scaling the β_i emissivities:

$$\epsilon_i^{TES} = \beta_i \left(\frac{\epsilon_{min}}{\min(\beta_i)} \right) \quad (14)$$

An example HyTES LST and emissivity output image are shown in Figure 16 for a flight over Death Valley on 07/12/2014 at 6m spatial resolution showing from left; L1 Brightness Temperature - RGB Red Band 150 (10.1 µm), Green Band 100 (9.2 µm), and Blue Band 58 (8.5 µm), L2 Land Surface Temperature (LST), and L2 Emissivity - RGB Red Band 150 (10.1 µm), Green Band 100 (9.2 µm), and Blue Band 58 (8.5 µm). In the emissivity RGB image different colors correspond to different rock types, e.g. quartz is red, carbonates are white, quartz-poor rocks are black, and basalts are blue.

For pixels with low spectral contrast (e.g., graybody surfaces), the accuracy of MMD calculated from TES is compromised and approaches a value that depends on measurement error and residual errors from incomplete atmospheric correction. For ASTER, which has a NEΔT of 0.3 K at 300 K, measurement error contributes to the apparent contrast, and a method was explored to correct the apparent MMD using Monte Carlo simulations. For HyTES we expect measurement errors to be minimal and atmospheric effects to be the largest contribution to MMD errors. A further problem for graybody surfaces is a loss of precision for low MMD values. This is due to the shape of the power-law curve of ϵ_{min} vs. MMD at low MMD values, where small changes in MMD can lead to large changes in ϵ_{min}. To address these issues, the ASTER TEWG initially proposed a threshold classifier for graybody surfaces. If MMD<0.03, the value of ϵ_{min} in equation 12 was set to 0.983, a value typical for water and most vegetated surfaces. However, this classification was later abandoned as it introduced large step discontinuities in most images (e.g., from vegetation to mixed-cover types).

The consequence of removing the threshold classifier was that over graybody surfaces errors in emissivity could range from 0.01 to 0.05 (0.5 K to 3 K) due to measurement error and residuals errors from atmospheric correction (Gustafson et al. 2006; Hulley and Hook 2009b).

For HyTES, we expect to use original TES without classification and use the ISAC method to estimate the atmospheric parameters on a pixel-by-pixel basis.

For bare surfaces (rocks, soils, and sand), the error in NEM calculated T may be as much as 2–3 K, assuming a surface at 340 K due to the fixed assumption of ϵ_{max} = 0.96. This error can be corrected by recalculating T using the TES retrieved maximum emissivity, ϵ_{max}^{TES}, and the

atmospherically corrected radiances, R_i. The maximum emissivity used as correction for reflected $L_\lambda^\downarrow$ will be minimal.

$$T^{TES} = \frac{c_2}{\lambda_{max}}\left(ln\left(\frac{c_1\epsilon_{max}^{TES}}{\pi R_i \lambda_{max}^5} + 1\right)\right)^{-1} \quad (15)$$

In the original ASTER algorithm, a final correction is made for sky irradiance using the TES temperature and emissivities; however, this was later removed, as correction was minimal and influenced by atmospheric correction errors. This additional correction will not be used for HyspIRI.

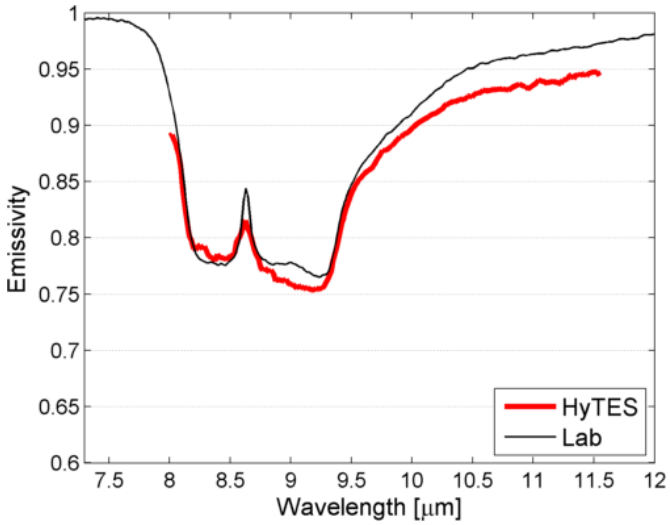

Figure 15: HyTES spectral emissivity using TES+ISAC retrieval for window bands 28-229 (8-11.5 micron) at the Algodones, CA at 3-km AGL matches closely in spectral shape with laboratory spectra (black) of sand samples collected at Algodones and measured in the lab using a Nicolet spectrometer.

Figure 15 shows an example of a HyTES retrieved emissivity spectra for bands 28-229 (8-11.5 micron) at the Algodones Dunes validation site in southeastern USA. The Algodones dunes consist primarily of quartz sands, which is evident by the quartz doublet between 8-9.5 micron in Figure 13. The HyTES spectra match closely in spectral shape with lab measured spectra (black) of sand samples collected at Algodones on past validation campaigns.

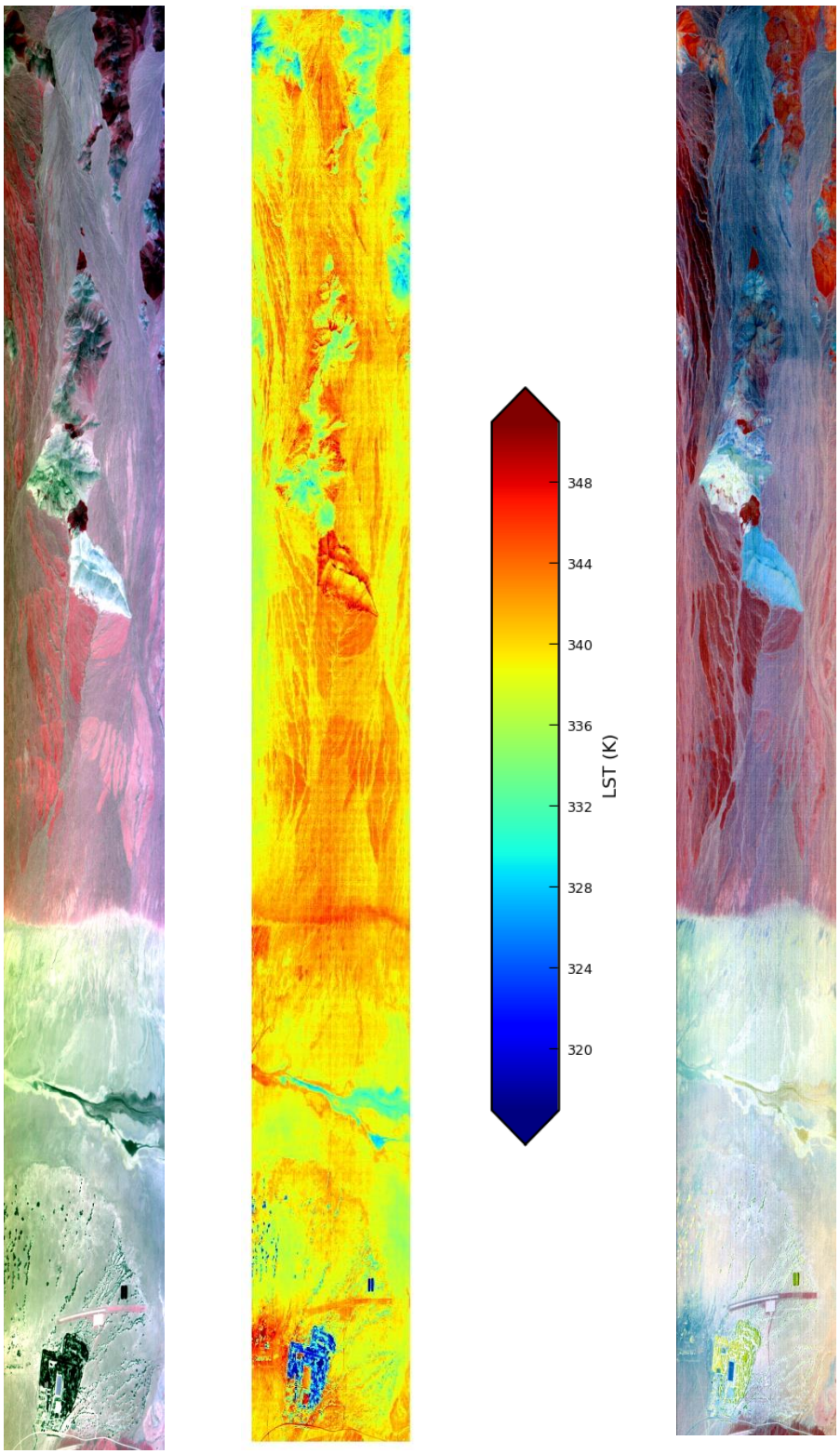

Figure 16. HyTES images at Death Valley on 07/12/2014 at 6m spatial resolution showing from left; L1 Brightness Temperature - RGB Red Band 150 (10.1 µm), Green Band 100 (9.2 µm), and Blue Band 58 (8.5 µm), L2 Land Surface Temperature (LST), and L2 Emissivity - RGB Red Band 150 (10.1 µm), Green Band 100 (9.2 µm), and Blue Band 58 (8.5 µm).

5.9 HyTES Principal Component (PC) Regression Emissivity

The HyTES standard L2 product only retrieves emissivity for the 'atmospheric window' bands 28-229 (8-11.5 micron) in order to minimize the effects of atmospheric attenuation. In order to obtain emissivity for the remaining HyTES bands covering the 7.4-12 micron, a statistical principal component (PC) regression method is employed. HyTES emissivity in the 7.4-8 micron region for example is necessary as input as first guess in the HyTES methane quantitative retrieval algorithm (Kuai et al. 2016).

The basic idea behind PC regression involves expressing the emissivity as a linear combination of a limited number of eigenfunctions derived from a set of selected laboratory spectra. The relevant number of components is determined by looking at the percentage of variance explained by the PCs. To generate the eigenfunctions we used 142 samples emissivity spectra from the ASTER spectral library that were measured in JPL using Nicolet 520 Fourier transform infrared spectrometer (Baldridge et al. 2009). Estimates of emissivity, $\boldsymbol{\varepsilon}$, using the PC regression onto the relevant eigenvectors of the emissivity dataset can be obtained as :

$$\boldsymbol{\varepsilon} = \boldsymbol{c}\, U(\nu_{hsr}), \tag{16}$$

where $\boldsymbol{c}$ is the PCA coefficient vector, and $U(\nu_{hsr})$ is the matrix of the first *n* eigenvectors of the lab emissivity spectra consisting of sand dunes, soils veg and rocks emissivities etc. and ν_{hsr} are the wavenumbers of the desired emissivity. The principal components of 142 laboratory spectra at 1cm^{-1} resolution between 830 –1500cm^{-1} were regressed against the response functions of the 256 HyTES bands. The first eight eigenfunctions could explain about 98% variability in the emissivity spectra matrix, and therefore n = 8 was selected for data reduction. The PCA coefficient vector $\boldsymbol{c}$, in equation 15 is obtained by:

$$\boldsymbol{c} = \boldsymbol{\varepsilon}(\boldsymbol{\nu})\, \boldsymbol{A}^{\boldsymbol{T}}\, (\boldsymbol{A}\, \boldsymbol{A}^{\boldsymbol{T}})^{-\mathbf{1}} \tag{17}$$

Where, $\boldsymbol{\varepsilon}(\boldsymbol{\nu})$ is the input HyTES emissivity $\boldsymbol{A}$ is the matrix obtained by convolving HyTES sensor response function with the first eight eigenvectors of U. Figure 17 shows an example of the PC regression approach in equation 15 applied to retrieved HyTES emissivity spectra (red) at the Algodones Dunes, CA, where the blue line is the estimated PC regression emissivities for the full HyTES wavelength range from 7.4-12 microns. The PC emissivities closely match the overall spectral shape of the original retrieved spectra and extend these values below 8 and above 11.5 micron based on the shape of the input emissivity and the laboratory derived eigenfunctions.

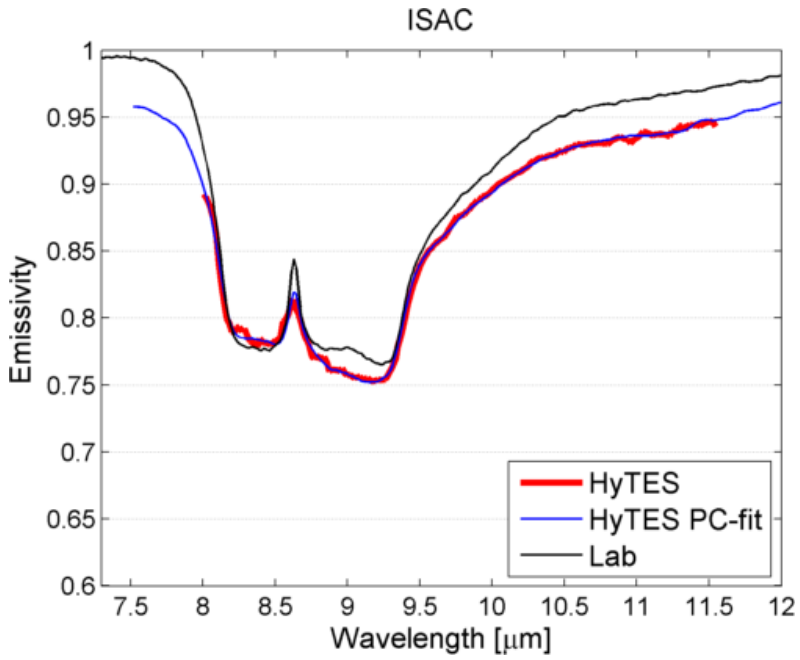

Figure 17: HyTES spectral emissivity using TES+ISAC retrieval for window bands 28-229 (8-11.5 micron) at the Algodones, CA at 3-km AGL matches closely in spectral shape with laboratory spectra (black) of sand samples collected at Algodones and measured in the lab using a Nicolet spectrometer.

5.10 Validation: Cuprite

The Cuprite area is located on the western edge of Esmeralda Country, Nevada, about 25 km south of the town of Goldfield. The area is divided by U.S. Highway 95. Figure 18 shows a HyTES Radiance image over Cuprite, Nevada with bands 150, 100, 75 displayed as RGB and retrieved emissivity spectra. These bands are typically used to highlight variations in silicate rocks. The area shown in the image is dominated by Tertiary volcanics and Quaternary deposits. Sections of the Tertiary volcanics were intensely altered by a hydrothermal system during mid to late Miocene time. Ashley and Abrams (1978) divided the hydrothermal alteration into three field-mappable zones: silicified rocks, opalized rocks (opalite), and argillized rocks. The alteration has a concentric pattern, with the silicified zone forming a circular core surrounded by opalized and then argillized rocks. Detailed descriptions of the alteration zones can be found in (Ashley and Abrams 1978).

Example spectra extracted from the HyTES data together with laboratory spectra from field samples are shown in Figure 18. The laboratory spectra were measured using the JPL Nicolet spectrometer. A detailed description of how the measurements were made is given in Baldridge et al. 2009.

The spectra for areas A and C correspond to regions dominated by Alunite and Kaolinite and have a broad minima centered around 9 um typically of these clay minerals. Previous studies using multispectral thermal infrared airborne imaging systems were unable to separate these minerals (Hook et al. 1992), however, the higher spectral "hyperspectral" resolution makes this easily possible (Figure 18 – spectra). It is also worth noting that with these previous multispectral systems a combination of 3 spectral bands of the radiance data displayed as an RGB image appeared gray in color. This was because the spectrally broad bands were highly correlated and resulted in the development of the decorrelation stretch which highlights the subtle emissivity variations masked by the more dominant temperature variations. In the HyTES image, this is not necessary as the narrow spectral bands capture far greater contrast and allow minerals to be identified based on their spectral features. This situation is analogous to reflective measurements where a spectrally broad band can only be used to discriminate groups of minerals whereas narrow spectral bands can be used to identify minerals. For example the spectrally broad band on the Landsat sensor around 2.2 μm can be used to distinguish clay rich altered areas but higher spectral resolution is needed to identify the presence of Alunite and Kaolinite with instruments like AVIRIS. In the thermal infrared broad band sensors like ASTER allow discrimination of clay minerals but high spectral resolution systems like HyTES are needed to identify the minerals that are present.

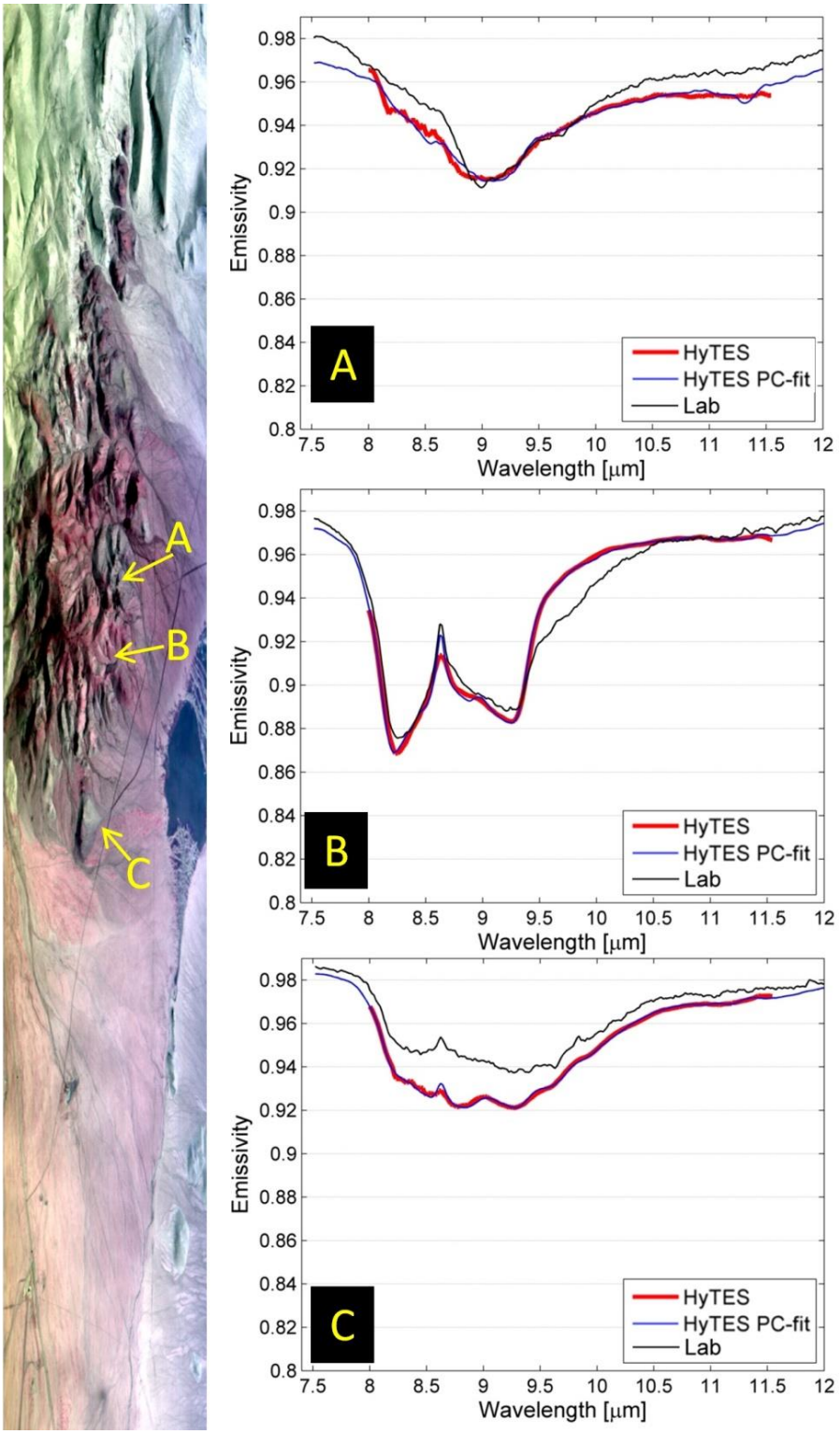

Figure 18. HyTES Radiance image over Cuprite, Nevada with bands 150, 100, 75 displayed as RGB and retrieved emissivity spectra over areas consisting of Alunite (A), Quartz (B), and Kaolinite (C). TES retrieved spectra for the window bands are shown in red, a Principal-Component (PC) regression fit to the TES data covering all wavelengths are shown in blue, and lab spectra of samples collected in these areas are in black.

6 References

Ashley, R.P., & Abrams, M.J. (1978). Mapping of Limonite, Clay Mineral, and Alunite Contents of Hydrothermally Altered Rocks in Cuprite Mining District, Nevada, Using Aircraft Scanner Imagery for 0.46-2.36 Mum Spectral Region. *Economic Geology, 73*, 307-307

Baldridge, A.M., Hook, S.J., Grove, C.I., & Rivera, G. (2009). The ASTER Spectral Library Version 2.0. *Remote Sensing of Environment, 114*, 711-715

Barducci, A., & Pippi, I. (1996). Temperature and emissivity retrieval from remotely sensed images using the "grey body emissivity" method. *Ieee Transactions on Geoscience and Remote Sensing, 34*, 681-695

Barton, I.J., Zavody, A.M., Obrien, D.M., Cutten, D.R., Saunders, R.W., & Llewellyn-Jones, D.T. (1989). Theoretical Algorithms for Satellite-Derived Sea-Surface Temperatures. *Journal of Geophysical Research-Atmospheres, 94*, 3365-3375

Becker, F., & Li, Z.L. (1990). Temperature-Independent Spectral Indexes in Thermal Infrared Bands. *Remote Sensing of Environment, 32*, 17-33

Borbas, E., Knuteson, R., Seemann, S.W., Weisz, E., Moy, L., & Huang, H. (2007). A high spectral resolution global land surface infrared emissivity database. In, *Joint 2007 EUMETSAT Meteorological Satellite &15th AMS Satellite Meteorology and Oceanography Conference*. Amsterdam, The Netherlands

Brown, O., & Minnett, P. (1999). MODIS infrared sea surface temperature algorithm. *Algorithm Theoretical Basis Document Version 2*, Univ. of Miami, Miami, Fla.

Coll, C., & Caselles, V. (1997). A split-window algorithm for land surface temperature from advanced very high resolution radiometer data: Validation and algorithm comparison. *Journal of Geophysical Research-Atmospheres, 102*, 16697-16713

Deschamps, P.Y., & Phulpin, T. (1980). Atmospheric Correction of Infrared Measurements of Sea-Surface Temperature Using Channels at 3.7, 11 and 12 Mu-M. *Boundary-Layer Meteorology, 18*, 131-143

Gillespie, A., Rokugawa, S., Hook, S., Matsunaga, T., & Kahle, A.B. (1999). Temperature/Emissivity Separation Algorithm Theoretical Basis Document, Version 2.4, ASTER TES ATBD, NASA Contract NAS5-31372, 31322 March, 31999

Gillespie, A., Rokugawa, S., Matsunaga, T., Cothern, J.S., Hook, S., & Kahle, A.B. (1998). A temperature and emissivity separation algorithm for Advanced Spaceborne Thermal Emission and Reflection Radiometer (ASTER) images. *Ieee Transactions on Geoscience and Remote Sensing, 36*, 1113-1126

Gustafson, W.T., Gillespie, A.R., & Yamada, G.J. (2006). Revisions to the ASTER temperature/emissivity separation algorithm. In, *2nd International Symposium on Recent Advances in Quantitative Remote Sensing*. Torrent (Valencia), Spain

Hook, S.J., Gabell, A.R., Green, A.A., & Kealy, P.S. (1992). A Comparison of Techniques for Extracting Emissivity Information from Thermal Infrared Data for Geologic Studies. *Remote Sensing of Environment, 42*, 123-135

Hulley, G.C., & Guillevic, P. (2015). Novel In-Scene Atmospheric Correction Techniques for the Airborne Hyperspectral Thermal Emission Spectrometer (HyTES). *Journal of Geophysical Research, In Preparation*

Hulley, G.C., Guillevic, P., Vance, N., Rivera, G., Hook, S.J., Radocinski, R.G., Grigsby, S., & Roberts, D.A. (2014). HyspIRI-MASTER-HyTES Land Surface Temperature and Emissivity Products and Enhancements. In, *HyspIRI Science and Applications Workshop*. Pasadena, CA

Hulley, G.C., & Hook, S.J. (2009a). Intercomparison of Versions 4, 4.1 and 5 of the MODIS Land Surface Temperature and Emissivity Products and Validation with Laboratory Measurements of Sand Samples from the Namib Desert, Namibia. *Remote Sensing of Environment, 113*, 1313-1318

Hulley, G.C., & Hook, S.J. (2009b). The North American ASTER Land Surface Emissivity Database (NAALSED) Version 2.0. *Remote Sensing of Environment*, 1967-1975

Hulley, G.C., Hook, S.J., Abbott, E., Malakar, N., Islam, T., & Abrams, M. (2015). The ASTER Global Emissivity Database (ASTER GED): Mapping Earth's emissivity at 100 meter spatial scale. *Geophysical Research Letters, 42*, doi:10.1002/2015GL065564

Hulley, G.C., Hook, S.J., & Baldridge, A.M. (2008). ASTER land surface emissivity database of California and Nevada. *Geophysical Research Letters, 35*, L13401, doi: 13410.11029/12008gl034507

Jimenez-Munoz, J.C., & Sobrino, J.A. (2010). A Single-Channel Algorithm for Land-Surface Temperature Retrieval From ASTER Data. *Ieee Geoscience and Remote Sensing Letters, 7*, 176-179

Kealy, M.J., Montgomery, M., & Dovidio, J.F. (1990). Reliability and Predictive-Validity of Contingent Values - Does the Nature of the Good Matter. *Journal of Environmental Economics and Management, 19*, 244-263

Kealy, P.S., & Hook, S. (1993). Separating temperature & emissivity in thermal infrared multispectral scanner data: Implication for recovering land surface temperatures. *Ieee Transactions on Geoscience and Remote Sensing, 31*, 1155-1164

Kneizys, F.X., Abreu, L.W., Anderson, G.P., Chetwynd, J.H., Shettle, E.P., Berk, A., Bernstein, L.S., Robertson, D.C., Acharya, P.K., Rothman, L.A., Selby, J.E.A., Gallery, W.O., & Clough, S.A. (1996). The MODTRAN 2/3 Report & LOWTRAN 7 Model, F19628-91-C-0132. In, *Phillips Lab*. Hanscom AFB, MA

Kuai, L., Hulley, G.C., Worden, J., Li, K.-F., Hook, S.J., Duren, R., Guillevic, P., Johnson, W., Mihaly, J., Eng, B.T., Chazanoff, S., Vance, N., & Rivera, G. (2016). Characterization of anthropogenic methane plumes with the Hyperspectral Thermal Emission Spectrometer (HyTES): a retrieval method and error analysis. *Atmospheric Measurement Techniques, doi:10.5194/amt-2015-402, in review*

Li, F.Q., Jackson, T.J., Kustas, W.P., Schmugge, T.J., French, A.N., Cosh, M.H., & Bindlish, R. (2004). Deriving land surface temperature from Landsat 5 and 7 during SMEX02/SMACEX. *Remote Sensing of Environment, 92*, 521-534

Lyon, R. (1965). Analysis of ROcks by Spectral INfrared Emission (8 to 25 microns). *Economic Geology and the Bulletin of the Society of Economic Geologists, 60*, 715-736

Masuda, K., Takashima, T., & Takayama, Y. (1988). Emissivity of Pure and Sea Waters for the Model Sea-Surface in the Infrared Window Regions. *Remote Sensing of Environment, 24*, 313-329

Matsunaga, T. (1994). A temperature-emissivity separation method using an empirical relationship between the mean, the maximum, & the minimum of the thermal infrared emissivity spectrum, in Japanese with English abstract. *Journal Remote Sensing Society Japan, 14*, 230-241

Norman, J.M., & Becker, F. (1995). Terminology in Thermal Infrared Remote-Sensing of Natural Surfaces. *Agricultural and Forest Meteorology, 77*, 153-166

Prata, A.J. (1994). Land-Surface Temperatures Derived from the Advanced Very High-Resolution Radiometer and the Along-Track Scanning Radiometer .2. Experimental Results and Validation of Avhrr Algorithms. *Journal of Geophysical Research-Atmospheres, 99*, 13025-13058

Price, J.C. (1984). Land surface temperature measurements from the split window channels of the NOAA 7 Advanced Very High Resolution Radiometer. *Journal of Geophysical Research, 89*, 7231-7237

Snyder, W.C., Wan, Z., Zhang, Y., & Feng, Y.Z. (1998). Classification-based emissivity for land surface temperature measurement from space. *International Journal of Remote Sensing, 19*, 2753-2774

Wan, Z.M., & Dozier, J. (1996). A generalized split-window algorithm for retrieving land-surface temperature from space. *Ieee Transactions on Geoscience and Remote Sensing, 34*, 892-905

Wan, Z.M., & Li, Z.L. (1997). A physics-based algorithm for retrieving land-surface emissivity and temperature from EOS/MODIS data. *Ieee Transactions on Geoscience and Remote Sensing, 35*, 980-996

Watson, K. (1992). Spectral Ratio Method for Measuring Emissivity. *Remote Sensing of Environment, 42*, 113-116

Watson, K., Kruse, F.A., & Hummermiller, S. (1990). Thermal Infrared Exploration in the Carlin Trend, Northern Nevada. *Geophysics, 55*, 70-79

Young, S.J., Johnson, B.R., & Hackwell, J.A. (2002). An in-scene method for atmospheric compensation of thermal hyperspectral data. *Journal of Geophysical Research-Atmospheres, 107*

Yu, Y., Privette, J.L., & Pinheiro, A.C. (2008). Evaluation of split-window land surface temperature algorithms for generating climate data records. *Ieee Transactions on Geoscience and Remote Sensing, 46*, 179-192